Experimental and numerical investigation on the accuracy of phosphor particle streak velocimetry

Luming Fan, Patrizio Vena, Bruno Savard, Benoît Fond

Experimental and numerical investigation on the accuracy of phosphor particle streak velocimetry

Luming Fan[a,b], Patrizio Vena[a], Bruno Savard[b], Benoît Fond[c,*]

[a] *Aerospace Research Centre, National Research Council Canada, 1200 Montreal Road, Ottawa, ON K1A 0R6, Canada*

[b] *Department of Mechanical Engineering, Polytechnique Montréal, Montréal, QC H3T 1J4, Canada*

[c] *ONERA - The French Aerospace Lab, 8 rue des Vertugadins, 92190 Meudon, France*

Abstract

A new Phosphor Particle Streak Velocimetry (phosphor-PSV) diagnostic with high spatial resolution was recently demonstrated [1], where individual phosphor particles, excited by a short pulse laser, form streaks as a results of their displacement by the flow during their relatively long luminescence decays. The local flow velocity is derived by fitting each phosphor streak as a two-dimensional linearly-moving point source with a mono-exponential decaying emission. This single-pulse, single-exposure technique yields, as in particle tracking velocimetry, a vector for each particle, avoiding the spatial filtering associated with particle image velocimetry (PIV). The wavelength-shifted luminescence also allows rejection of unwanted reflected laser light and macroscopic measurements in [1] were obtained at a distance of 30 μm from the wall. In this manuscript, we establish by a combination of experiments and luminescent particle imaging simulation the performance of the technique in a range of flow conditions, and imaging parameters. A new image segmentation algorithm is developed and applied to ~~particle~~ phosphor streak images to

*Corresponding author:
Email address: benoit.fond@onera.fr (Benoît Fond)

improve the density of measurements to 0.004 ~~streaks~~vectors per pixel. ~~, about 4 times higher than the vector density obtained by a 32 × 32 px interrogation window PIV.~~ Two phosphors with decay times of 564.2 μs ($Gd_2O_2S:Tb^{3+}$) and 0.92 μs ($BaMgAl_{10}O_{17}:Eu^{2+}$), respectively are used to perform measurements in slow liquid flows (< 20 cm/s) and fast turbulent jets (up to 85 m/s). To assess the uncertainty of the approach for various experimental parameters (phosphor particles, flow velocity, particle image size, signal-to-noise ratio, and streamline curvature), synthetic streaks are generated and validated against experimental data. Finally, the impact of out-of-plane motion is investigated experimentally. This study paves the way for a wide implementation of the new phosphor-PSV technique in flow research and in particular to study two-phase flows and confined or semi-confined flows near solid boundaries.
Keywords: phosphor particles, velocimetry, PTV, PSV, uncertainty

---

ORCIDs

Luming Fan 0000-0002-9856-4853

Patrizio Vena 0000-0003-4463-7719

Bruno Savard 0000-0002-6989-8942

Benoit Fond 0000-0002-8152-4126

1. Introduction

Over the past three decades, Particle image velocimetry (PIV) has been successfully applied to measure velocity fields in a wide range of liquid and gaseous flows. In PIV, the particle displacement field is obtained by cross-correlating the intensity distribution of particle images formed by tracer particles during two consecutive light pulses separated by a short (and case-specified) time delay. Assuming these particles

have a sufficiently small Stokes number, they follow the instantaneous flow motion accurately. Each PIV vector is calculated based on the displacement of particles within a small area, known as the interrogation window. PIV yields instantaneous vector fields in a fixed grid of coordinates, hence is a Eulerian approach. The size of the window defines the spatial resolution, as the window-base correlation acts as a low-pass spatial filter on the velocity field. Measuring with PIV the velocity field in a thin boundary layer, or a highly turbulent flame, where steep velocity gradients can be expected, may yield compromised results, if there is a significant velocity gradient within the interrogation window.

In those cases, particle tracking velocimetry (PTV) may be used as an alternative, where each particle produces a local velocity vector, to yield high vector density to resolve the small-scale flow motion. For example, Kähler and co-workers [2] analysed the synthetic particle images in a given flow field and showed that the near-wall velocity profile obtained by the window-based correlation method (PIV) was always biased to a larger value due to the presence of velocity gradient as well as inhomogeneous particle distribution, whereas PTV provided an unbiased result for the same conditions. Yet, PTV requires particle searching algorithm to find the same particle image on the second frame and ambiguities may arise at high seeding densities. If PTV vector fields are obtained in rapid succession, for example using kHz lasers and cameras, then particle trajectories can be derived, and the motion of each particle can be expressed as a function of time, making this technique a Lagrangian approach. Perhaps most attractively, flow acceleration and potentially the pressure field can also be resolved from the Lagrangian approach, for example, using the recently emerged Shake-the-box technique [3].

To complement the PTV, in a previous letter [1], we introduced a new Lagrangian particle tracking method using phosphor particle tracers, which we named Phosphor

Particle Streak Velocimetry (phosphor-PSV). Prior to phosphor-PSV, there have been several studies exploiting the luminescence of phosphor particles for velocity measurements, which can be categorized into two routines:

- A fast decay phosphor with $\tau \ll \tau_k$, where τ is the $1/e$ emission decay time and τ_k is the smallest time scale of the flow motion, is used together with a double pulse UV laser to excite the particles, and a PIV camera, e.g., [4].

- Single-pulse UV excitation of a long-decay-time phosphor $\tau \gg \tau_k$, is used with a high-speed camera running at an ultra high frame rate to capture instantaneous particle positions marked by the slowly decaying emission, which are then used to perform series-PIV [5]. Since the high frame rate limits the frame size, the high-speed camera can be replaced by an ICCD camera operating at double-pulse mode, both frames are gated by a fast intensifier to maintain particle images as circular spots [6].

The former approach requires the use of a double-pulse UV laser, while the latter needs a specialised camera. Unlike the two routines described above, the phosphor-PSV proposed in our letter used phosphors whose decay time is comparable to the flow smallest time scale $\tau \sim \mathcal{O}(\tau_k)$. The emission from these phosphor particles lasts much longer than Mie scattering from a pulsed laser and decays exponentially with time, produces light streaks that mark the flow motion, which are recorded by a camera operating at a long exposure time. These streaks contain local velocity information which can be extracted by applying to each streak a two-dimensional fit describing a linearly moving point source with a mono-exponential decaying emission. In the letter [1], we demonstrated the phosphor PSV concept in an open air jet using a tin-doped phosphor $(Sr,Mg)_3(PO_4)_2{:}Sn^{2+}$ and validated it against simultaneous PIV/PTV, showing good agreement. The phosphor-PSV technique was

further applied to measure a laminar boundary layer that was less than 300 μm in thickness. The steep velocity gradient was successfully resolved, and the measured velocity profile across the boundary layer matched well with the Blasius solution. The vector closest to the wall was measured a distance of merely 30 μm away. In addition to absence of low-pass spatial filtering offered by tracing individual particles, some other apparent advantages of phosphor-PSV come from the use of an emission spectrally shifted from the incoming laser light, which includes, for example, avoiding strong laser reflection from a solid boundary in the same work, and separating different phases in two-phase flows [7]. Moreover, phosphors have been widely used for surface and flow temperature measurements, as reviewed in [8, 9]. Hence, the PSV technique we proposed also has the potential for simultaneous temperature and velocity measurements. For example, recently Deng and co-workers [10] used luminescent particles (PMMA doped with EuTTA) with an LED light and low-speed double-frame camera to perform simultaneous temperature and velocity measurements in a microfluidic chamber. A temperature precision better than 1 K was achieved by measuring the intensity ratio of the consecutive frames that recorded separately the rise and decay of the luminescent signal emitted from individual particles. This approach was valid given that the velocity does not exceed 0.5 mm/s in the reported configuration such that circular particle images are maintained in each frame. Beyond that velocity range, streaks start to form due to persistent excitation and a long exposure, hence limiting the technique to microfluidic applications where flow speed is extremely low. However, this limit may be overcome by treating the streak with the PSV technique proposed in the present study. Despite the clear potential to measuring local flow temperature simultaneously with PSV, we focus in this study on exploiting phosphor particles for velocity measurements at room temperature..

The goal of the present paper is to assess the range of flow conditions for the technique using different phosphor materials, and to assess the measurement uncertainty, including some specific cases (high vorticity, out-of-plane motion). In the following we first describe the principle and methodology of phosphor PSV, including an improved image segmentation method for high streak densities and details of the 2D least square fitting. Then we report the experimental results acquired with two additional phosphor materials under different velocity ranges according to their emission decay characteristics. We also conduct uncertainty analysis by generating virtual phosphor streaks with random noise and retrieving their input velocity. Finally, the potential influences of out-of-plane motion and curved streamlines on the velocity measurement are experimentally addressed.

2. Methods

2.1. Mathematical description of phosphor PSV

In this section, we recall and expand the principle of phosphor particle streak velocimetry by deriving the intensity profile of a moving particle with exponentially decaying emission. We start with the intensity distribution $I(x, y)$ of a still phosphor particle exited by UV light, which follows a 2D Gaussian distribution on the image plane:

$$I(x, y) = I_0 \cdot \exp\left[-\frac{(x - x_0)^2 + (y - y_0)^2}{2\sigma^2}\right] \tag{1}$$

where I_0 is the intensity constant, x_0, y_0 are the particle initial position, and σ is the particle size constant. If the emission intensity of the luminescent light spot follows a mono-exponential decay, and the particle moves at a velocity (v_x, v_y) (in pixel/s), the intensity distribution of the moving particle image reads:

$$I(x, y, t) = I_0 \cdot \exp(-t/\tau) \cdot \exp\left[-\frac{(x - x_0 - v_x t)^2 + (y - y_0 - v_y t)^2}{2\sigma^2}\right] \tag{2}$$

where τ is the $1/e$ decay time of the phosphor, and can be characterised using a Photomultiplier tube (PMT). Expanding and recombining the terms on the RHS gives

$$I(x, y, t) = I_0 \cdot \exp\left(at^2 + bt + c\right) \tag{3}$$

We define the particle displacement (in pixels) during the $1/e$ decay time as $\Delta x = v_x\tau$, $\Delta y = v_y\tau$. Then

$$a = \frac{\Delta x^2 + \Delta y^2}{2\sigma^2\tau^2} \tag{4}$$

$$b = \frac{(x - x_0)\Delta x + (y - y_0)\Delta y}{\sigma^2\tau} - \frac{1}{\tau} \tag{5}$$

$$c = -\frac{(x - x_0)^2 + (y - y_0)^2}{2\sigma^2} \tag{6}$$

Assuming v_x, v_y remain constant during the decay time of the phosphor, integrating $I(t)$ from $t = 0$ to $t = +\infty$ ($a \neq 0$) gives

$$E(x, y) = \int_0^{+\infty} I_0 e^{-at^2+bt+c} \mathrm{d}t = \frac{I_0}{2}\sqrt{\frac{\pi}{a}} e^{\frac{b^2+4ac}{4a}} \left[\mathrm{erf}\left(\frac{b}{2\sqrt{a}}\right) + 1\right] \tag{7}$$

The above function gives the analytical expression of the image of a moving point light source during the persistence of luminescence emission. It has 6 parameters, including the two displacement components:

$$E(I_0, x_0, y_0, \sigma, \Delta x, \Delta y) \tag{8}$$

which can be determined by non-linear least square fitting against real phosphor streaks obtained from experiments. The velocity components v_x, v_y can be calculated from $v_x = \Delta x/\tau$, $v_y = \Delta y/\tau$ knowing the decay time τ. The reason for introducing the dimensionless (pixel) displacement into the expression instead of using velocities v_x, v_y directly is to facilitate comparisons among different phosphors and imaging

parameters. This is similar to PIV/PTV where errors are quantified by particle displacement, since the velocity, magnification factor, and measurement time can always be changed for case-specified flow conditions. In theory, Eq. (7) should be integrated over area of each pixel in order to reproduce the final pixelated streak image as recorded by a camera, but such integration is complex. However for a streak with a thickness of more than 2 pixels ($\sigma = 0.5$ pixel), the intensity distribution can be well approximated by evaluating Eq. (7) at the center coordinates of each pixel, as will be illustrated in Subsection 2.7. The thickness of a streak is evaluated by 4σ, similar to the particle image diameter in synthetic PIV images.

Note that some phosphor materials may exhibit decay behaviour which are multi-exponential, e.g., $CaTiO_3$:Pr^{3+} [11], with the expression

$$I(t) = I_1 \exp(-t/\tau_1) + I_2 \exp(-t/\tau_2). \tag{9}$$

If a single-exponential decay with an equivalent τ cannot be found to well approximate the curve, the multi-exponential feature can still be easily incorporated into the analytical expression by integrating the two parts separately, which does not increase the number of parameters for the particle streak fitting. Some previous synthetic particle image programs, e.g. [12], assumed independent σ_x and σ_y along different directions to account for elliptical particle image shape due to image distortion. This can also be applied to the analysis above, but will yield one more parameter in Eq. (8) and thus lead to longer processing times.

2.2. Optical measurement system

The optical setup for phosphor particle streak velocimetry is shown in Figure 1. A frequency-quadrupled single-pulse Nd:YAG laser (Quanta-Ray LAB-150) outputting

at 266 nm was used to excite phosphor particles. Two cylindrical lenses (focal length f = -25 mm and 150 mm) were carefully aligned to expand the beam and form a collimated light sheet, followed by another cylindrical lens f = 400 mm to narrow down the thickness. The weak outer edges of the Gaussian beam were then trimmed by a slit to avoid regions of low fluences associated with low SNR. The light sheet thickness in the imaging region of interest was 0.2 mm, measured using a traversing knife edge and a photodiode. The laser fluence was set to roughly 100 mJ/cm^2 to keep a sufficiently high signal-to-noise ratio for the measurements. A 16-bit scientific CMOS camera (Imager sCMOS from La Vision, 2560 $\times$ 2160 pixels, 6.5 μm pixel pitch size) equipped with a Tamron 60 mm $f/2$ Macro lens was used to image the particles. The projected spatial resolution in the object plane was 7.4 μm/pixel for the measurements in the cuvette and in the highly turbulent air jets, and 10.2 μm/pixel for the laminar/transitioning jets. The camera was operating in the rolling shutter mode to minimise readout noise: each row of pixels was exposed for 35 ms with a short delay to the previous row so that the common time during which all pixels were exposed was 5 ms. The UV laser pulse was fired within this time window to ensure the entire image field was captured. Since the luminescent emission in this study is much shorter than the common pixel time, the flow image is not distorted.

Table 1: A summary of the test conditions. Median sizes are provided by volume

Phosphor material	Abbreviation	Collecting wavelength (Filter)	Decay time	Median size	Flow condition
$Gd_2O_2S:Tb^{3+}$	GOS:Tb^{3+}	> 515 nm (Thorlabs FGL515S)	564.2 μs [13]	2.5 μm	stirred liquid cuvette 0-0.2 m/s
$(Sr,Mg)_3(PO_4)_2:Sn^{2+}$	SMP:Sn^{2+}	> 645 nm (Edmund Optics #66-097)	26.8 μs	1.94 μm [14]	air jet 0.2-12 m/s [1]
$BaMgAl_{10}O_{17}:Eu^{2+}$	BAM:Eu^{2+}	466-40 nm (Edmund Optics #86-363)	0.92 μs [15]	2.5 μm	air jet 20-85 m/s

Three different phosphor materials were chosen to measure different flow conditions, as summarized in Table 1. Particles of GOS:Tb^{3+} and BAM:Eu^{2+} were supplied by Phosphor Technology, both with a median size of 2.5 μm (by volume) as reported by the supplier. For SMP:Sn^{2+}, raw powder was ordered from OSRAM

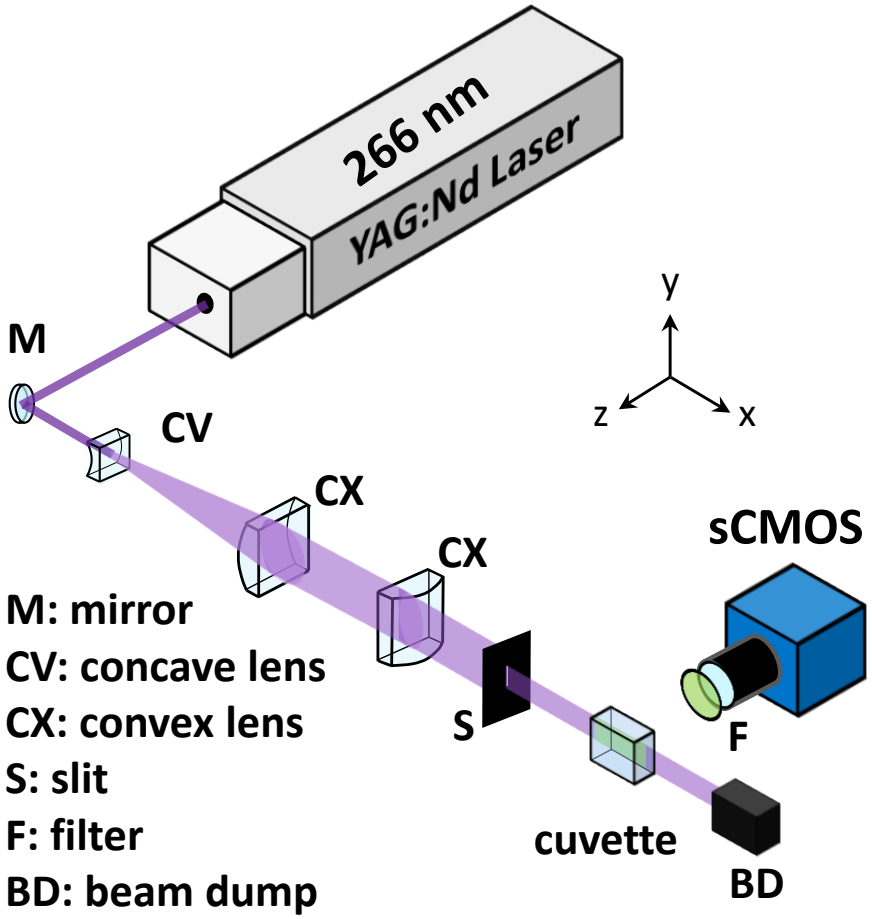

Figure 1: A schematic of optical setup. For some cases, the cuvette shown in this setup is placed by a 10 mm inner diameter air jet.

and then further ground to a median size of 1.94 μm [14]. GOS:Tb^{3+} was applied to measure the liquid flow speed in a stirred liquid cuvette (as shown in Figure 1), while SMP:Sn^{2+} and BAM:Eu^{2+} were used to trace an open air jet, but at different bulk velocity ranges according to their decay time. The emission spectra of three phosphors are shown in Figure 2. Emission of GOS:Tb^{3+} has multiple peaks, with the strongest at 545 nm which originates from the $^5D_4$ to $^7F_4$ transition, hence the emission of this phosphor appears a bright green colour. The decay time of this

emission peak is 564.2 μs at room temperature, so it is applied to measure slow liquid flows. Note that the blue emission peaks (below 500 nm) of GOS:Tb^{3+} have a much shorter decay time of 83.0 μs compared to the green peak. Hence, a 515 nm long-pass colour glass was placed in front of the camera lens to avoid a contribution from these short-lived emissions. SMP:Sn^{2+} has a broadband emission that appears orange in colour. The decay time is 26.8 μs and was found insensitive to temperature changes between 300-500 K [14]. BAM:Eu^{2+}, a frequently used blue emitting thermographic phosphor, has a short decay time around 1 μs at room temperature, hence is suitable for measuring fast flows. A previous study [15] has reported a bi-exponential decay consisting of a 270 ns faster decay mode and a 1 μs slow decay mode. The decay time of BAM:Eu^{2+} was found to vary with collection wavelength in that study, hence the emission decay curve measured around 460 nm (a 466 $\pm$ 40 nm filter was used) was extracted from [15]. A 2D mono-exponential fit to the synthetic streak images generated with the true decay curve was found to be best approximated by a mono-exponential decay with $\tau = 0.92$ μs. Note that for SMP:Sn^{2+} and BAM:Eu^{2+}, the same filters as for previous thermometry measurements were used [14, 16] (also for removing the 532 nm Mie scattering in the cases that simultaneous PIV was performed), yielding only 26% and 39% of the signal, respectively. For velocity measurements only, about 3-fold improvement in signal levels can be afforded by removing the filters.

2.3. Flow test cases

For the demonstration using GOS:Tb^{3+}, the powder was added to water at a set mass load and dispersed using an ultrasonic homogenizer (Bandelin Sonopuls HD 2200). The suspension was then diluted and filled into a 28 ml UV-fused silica cuvette (40 $\times$ 20 $\times$ 35 mm) containing a stirring bar (8 mm in length), and placed

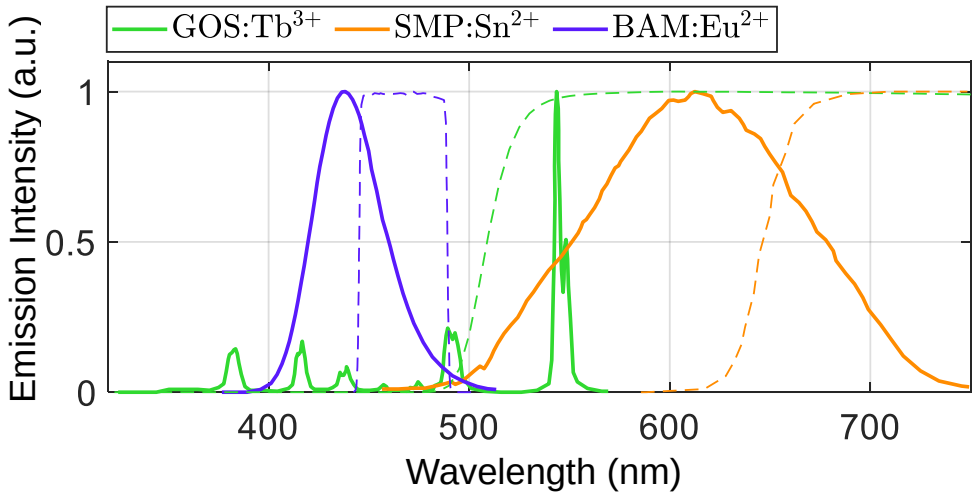

Figure 2: Normalized Emission spectrum measured at room temperature for GOS:Tb^{3+} reproduced from [13], SMP:Sn^{2+} [17], and BAM:Eu^{2+} [18]. The dashed lines are the transmission curve for the corresponding filters used. The line colours are chosen based on the apparent emission colour of that phosphor.

on a magnetic stirring plate. The flow was stirred at a constant angular speed ∼200 rpm during the measurement to drive the flow motion.

SMP:Sn^{2+} particles were tested in laminar and transitioning air jets from 0.2 to 12 m/s. The measurements were performed using two flow configurations: a 10 mm inner diameter round tube to produce air jets with axial velocities ranging from 2 to 12 m/s, and a 5 × 5 cm^2 long square tube with honey-comb to produce uniform velocity fields ranging from 0.2-1.25 m/s. Both tubes are 1 metre in length. PIV (32 × 32 px interrogation window, 0.33 × 0.33 mm^2) was performed simultaneously for validation. Only the jet flow was seeded with particles, while the ambient air remained unseeded.

For measurements using BAM:Eu^{2+}, the same 10 mm round jet was used, but with an axial velocity at 26, 65, and 85 m/s (Re = 16800, 42000, 55000), respectively. Again, only the jet flow was seeded. PIV was performed using the same phosphor

particles, and the PSV camera to capture a similar field of view (with the same magnification factor) by swapping the filter to a 532 ± 10 nm band pass filter. Due to the high-speed flow motion, the pulse interval was set to 2 μs and the interrogation window size was 64 × 64 px (0.47 × 0.47 mm^2).

To investigate the effect of the out-of-plane motion on the PSV technique, the 10 mm air jet with an axial velocity of 4.8 m/s was inclined by 5.6° and a 22° towards the camera, introducing a $v_z/v_y = 10\%$ and 40% out-of-plane motion, respectively. SMP:Sn^{2+} particles were used to perform the measurements.

In order to illustrate the formation of curved streaks, SMP:Sn^{2+} particles were dispersed into the same Re = 55000 highly turbulent jet instead of using BAM:Eu^{2+}. The former has a 30 times longer decay time than the latter, hence left long and curved streaks on the recorded imaged.

2.4. Streak segmentation method

Raw streak images are pre-processed, including object detection and segmentation, before applying a 2D fit to extract velocity components. Segmentation was previously implemented by detecting the orientation of each streak from the skeleton line and then determining the coordinates of a rectangular window which enveloped that streak [1]. In the present paper, we describe a new segmentation method based on image dilation, which can address much higher streak image densities. Image dilation is an elementary operation in morphological image processing, and is particularly useful for object edge detection such as large bubbles or particles in PIV applications [19]. The procedure is illustrated in the flowchart in Figure 3(a), and described as follows: ① a relatively high intensity threshold is applied to the image so that only the cores of the streaks are left; ② object detection is then performed to identify streak cores; ③ find the n^{th} streak core, ④ all neighbouring pixels connect-

ing to that core are searched on the raw image, and ⑤ judged one by one whether they belong to the streak. We used a combined criterion on pixel intensity and intensity gradient to exclude pixels that belong to background (intensity too low) or to another streak (positive intensity gradient); ⑥ add the identified pixels to the streak core; ⑦ repeat ④-⑥ to let the streak image gradually grow until final convergence is achieved (no more pixels satisfying the criterion can be found). Figure 3(b) shows the convergence of an example single streak. Since the streaks are grown from a small core, two streaks of small interspacing which are even partially overlapped can still be separated by this image dilation method, whereas finding a rectangle window to segment a single streak without cutting other streaks is no longer possible. The procedure for separating close streaks in a cluster is illustrated in Figure 3(c), and described as follows: at step ③, if an object contains significantly more pixels than a typical streak image, a higher intensity threshold was applied to detect whether more than one peak can be found in this object (a streak cluster). If yes, the objects found by the new threshold were allowed to grow from their own core at the same pace. After each loop, common pixels in any two objects were 'locked', i.e., no longer used to search connecting pixels in the following loops as they were identified as the boundary between those two objects.

2.5. Streak processing

In the cases of excessive seeding that may cause multiple scattering, or near-wall measurements, a baseline background noise may also contribute to the obtained streak intensity profile. Owing to the high spatial resolution of the imaging system used in this technique, the level of background signal is determined by setting a local intensity gradient threshold to determine the location where only background signal is present, and then subtracted from the streak image. Each streak is normalized

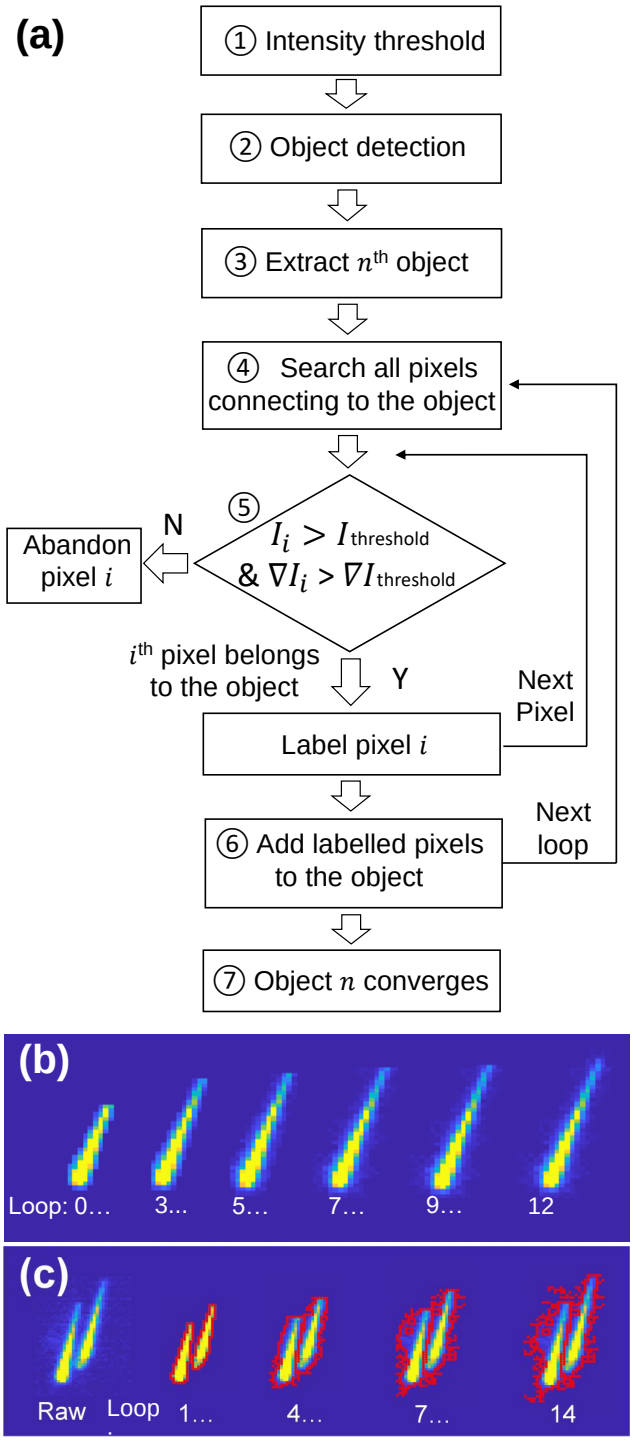

Figure 3: (a) Flowchart of the image dilation method for streak segmentation; (b) an example of converged single streak after 12 loops; (c) segmentation of two close streaks. The red line marks the boundary of each streak during dilation.

by its peak intensity prior to the 2D non-linear least square fitting. The fitting is implemented in Maltab by calling the `'lsqcurvefit'` function. In order to reduce the calculation time and increase the probability of the right fit, an initial guess of the six parameters in Eq. (8) is imposed, together with lower and upper bounds specified for those parameters. Otherwise, a local minimum in space may stop the search and lead to an erroneous fit. The pixel of maximum intensity is used as the initial guess for the particle start position (x_0, y_0). The initial guesses and bounds for I_0 and σ are determined by studying several sample streaks. The bounds of displacement $(\Delta x, \Delta y)$ are estimated based on the possible extreme values of velocity and can be quite loose. The fitting process is stopped automatically once any parameter hits the preset bounds, which is usually caused by a bad initial guess, bounds that are too wide, fully overlapped streaks, bad image quality, or incorrect streak segmentation (streak clusters). For the data collected in [1], those unsuccessful fits represented less than 5% of the total number of samples and were removed from the final results. With these steps, the in-plane flow velocity vector is extracted from a phosphor streak.

2.6. Measurements at high particle densities

We use a sample image of GOS:Tb^{3+}, Figure 4(a), taken in the stirred cuvette under high streak densities to illustrate the ability of the image segmentation technique to yield velocity measurements at relatively high seeding densities. Figure 4(b) presents an enlarged view of a 50 × 50 pixel (0.37 × 0.37 mm^2) area, and (c) superimposes all segmented streak, as well as the corresponding velocity vectors extracted from the 2D fitting. Although the streaks in this area show a high intensity contrast, which induces a variation in their apparent length on the image, the magnitude of the resulting vectors are close. This is due to the fact that the velocity is extracted

from the intensity decay in the fitting method, rather than the length of a streak. A spurious vector can be observed in Figure 4(c) pointing towards a different direction from all other vectors. This outstanding vector was attributed to unsuccessful separation of two close and weak peaks, which were both removed by the high universal intensity threshold during multiple-streak detection. This can be further improved by using an lower (adaptive) intensity threshold based on local peak intensity in that object, or pre-processing the streak cluster with a min-max filter if the intensities of the two streaks are too different. The apparently long streak in the bottom left corner consists of two streaks overlapping closely along the same line. The second vector was extracted by the algorithm as the entire intensity profile was preserved in that streak thanks to the gradient threshold whilst the first one lost half of the information after segmentation. Such streak clusters with more than 50% area overlap could potentially be processed by directly applying a multi-streak fitting:

$$E = E_1 + E_2 + ... + E_n \tag{10}$$

with four additional parameters $(I_i, x_i, y_i, \sigma_i)$ for every additional streak added to the fit. A same velocity (v_x, v_y) can be assumed for all streaks in this cluster. However, the computational time increases exponentially with more fitting parameters added to the function.

Figure 4 illustrates several advantages of using the fitting method over directly measuring the apparent length of each streak using for example an intensity threshold filter. Firstly, the direction of the velocity vector can be determined without any ambiguity since it is indicated by the decaying intensity. Secondly, the particle initial position x_0, y_0 obtained from the fitting has subpixel accuracy, similar to PIV where a 2D Gaussian fit, i.e., Eq. (1), is applied to determine the subpixel position

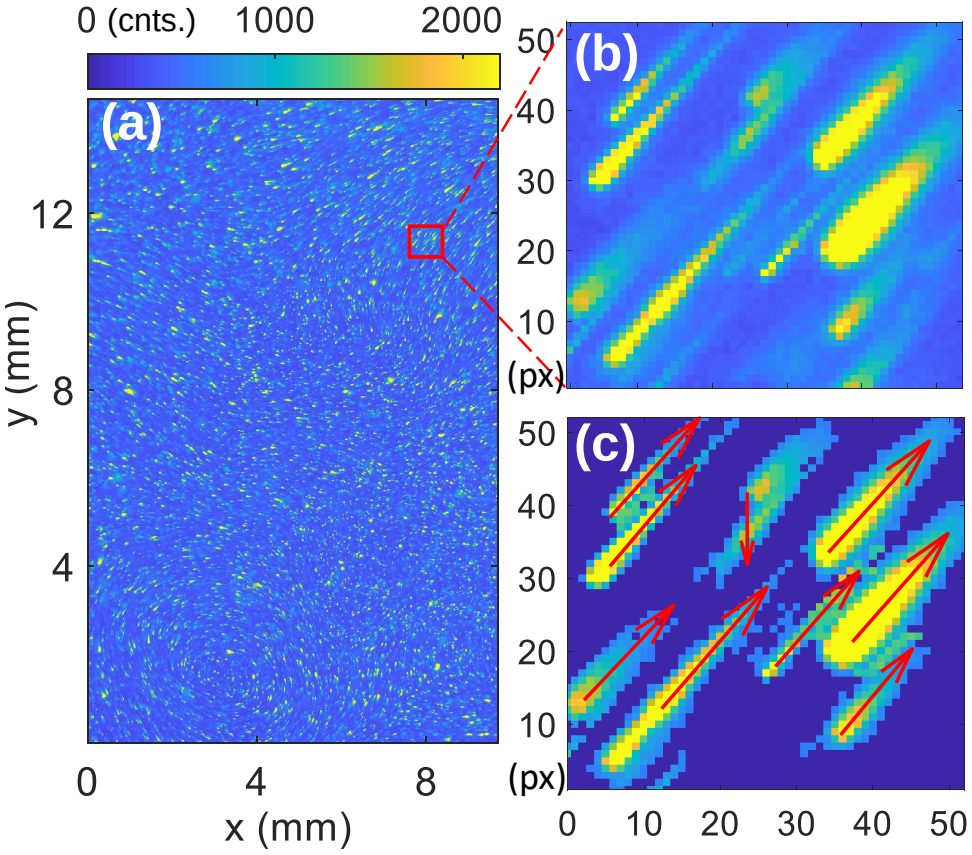

Figure 4: (a) An example image with a high streak density; (b) an enlarged view of an 0.37 × 0.37 mm^2 area; (c) individual streaks detected by the image dilation algorithm in this area, and the corresponding velocity vectors extracted from the 2D fitting.

for a circular light spot, known as the Gaussian estimator. This is particularly useful for streaks, regardless of whether they are of constant intensity or decaying intensity. In most cases, the start position x_0, y_0 is not located at the nearest end of the streak head, nor does it coincide with the pixel of highest counts. Instead, the particle starting position is usually located within one pixel upstream of the streak peak, because the number of photons collected by each pixel is also related to the particle residence time in the area covered by that pixel. Finally, the apparent length of a

streak would be highly susceptible to the inherent signal-to-noise ratio, or will not be able to separate a long streak cluster as shown in Figure 4(c). For the fitting method, however, the velocity is extracted from the intensity distribution imposed by the phosphor emission decay. Hence, even if the tail of a weak streak has already submerged in the noise and the length of the streak appeared much shorter than its noise-free counterpart, the velocity may still be extracted without much bias.

The minimum distance between two vectors in Figure 4(c) is only 7 pixels (the two vectors in the upper left corner), suggesting the algorithm can function with a theoretical ~~seeding density~~ streak image density of $1/(7 \times 20) \sim 0.007$ streak per pixel (spp), where 20 is the mean streak length in pixels. Similar to the particle image density (ppp) in PIV/PTV, the unit of streak image density is defined as the number of streaks per pixel (spp). For comparison, a 32×32 px interrogation window PIV leads to a vector density $\sim$0.001 vectors per pixel, as the window-based cross-correlation algorithm in PIV would apply low-pass filtering with respect to the vector field measured by techniques based on individual particle such as PSV and PTV. In practice, seeding particles are not uniformly distributed in the flow, such that the overall vector density in Figure 4(c) is 0.004 vector per pixel, still $\sim$5 times higher than the maximum density achieved by the window-based segmentation method in the previous study. This number is inversely proportional to the streak length (or velocity), and also slightly decreases with a larger streak thickness σ. Note that each streak covers 50-200 pixels, below which the fit quality may be compromised. Therefore an ultimate upper limit can be expected on the vector density of phosphor-PSV; about 0.005-0.01 vectors per pixel, when the image frame is entirely filled with streaks without any background pixels. This intrinsic limit can only be surpassed by adopting multi-streak fitting. In PTV, however, each particle covers less pixels, so the particle image density could be higher. Densities higher than 0.05 ppp have

been achieved in PTV [20].

2.7. Virtual streak generator

Similar to PIV, the uncertainty of phosphor-PSV is investigated by generating synthetic phosphor streaks with random noise, and then retrieving the input velocity from those streaks. There are two possible ways to generate a virtual phosphor streak image, as illustrated in Figure 5(a),(b). The first method evaluates the analytical intensity profile $E(x, y)$ defined in Eq. (7) at each pixel center location. For large particle image diameter, this is an excellent approximation for the pixelated image, in which each pixel count should be the integration of the Eq. (7) over the extent of each pixel. This is illustrated in Fig. 5(c), where both distributions are compared. However, when the thickness of the streak is around or below one pixel, the two distributions differ as illustrated in Figure 5(d). For reproducing such narrow intensity profiles, the second method is required: a finite time method where numerous instantaneous circular particle images are generated along the trajectory of the particle at a time step of 0.001τ with varying intensity as a function of time and then superimposed to form the streak for a time period of 4τ, beyond which the emission is negligible ($e^{-4}I_0$). The circular particle images are obtained by integrating a 2D Gaussian function, i.e., Eq. (1), over each pixel area $\mathrm{d}x\mathrm{d}y$, which yields an expression consisting of error functions, see [12]. The second method requires more computational resources: generating the streak in Figure 5(a) only used 8 ms, whilst (b) took 495 ms on a desktop PC for the time step used. Besides the thin streak case, the finite time method is also more appropriate to provide synthetic streak images in cases of very short displacement, or curved streaks. Apart from those cases, the virtual streaks simulated by both methods yield very similar results, as shown in Figure 5(c). In the simulations presented in this paper, the finite time method

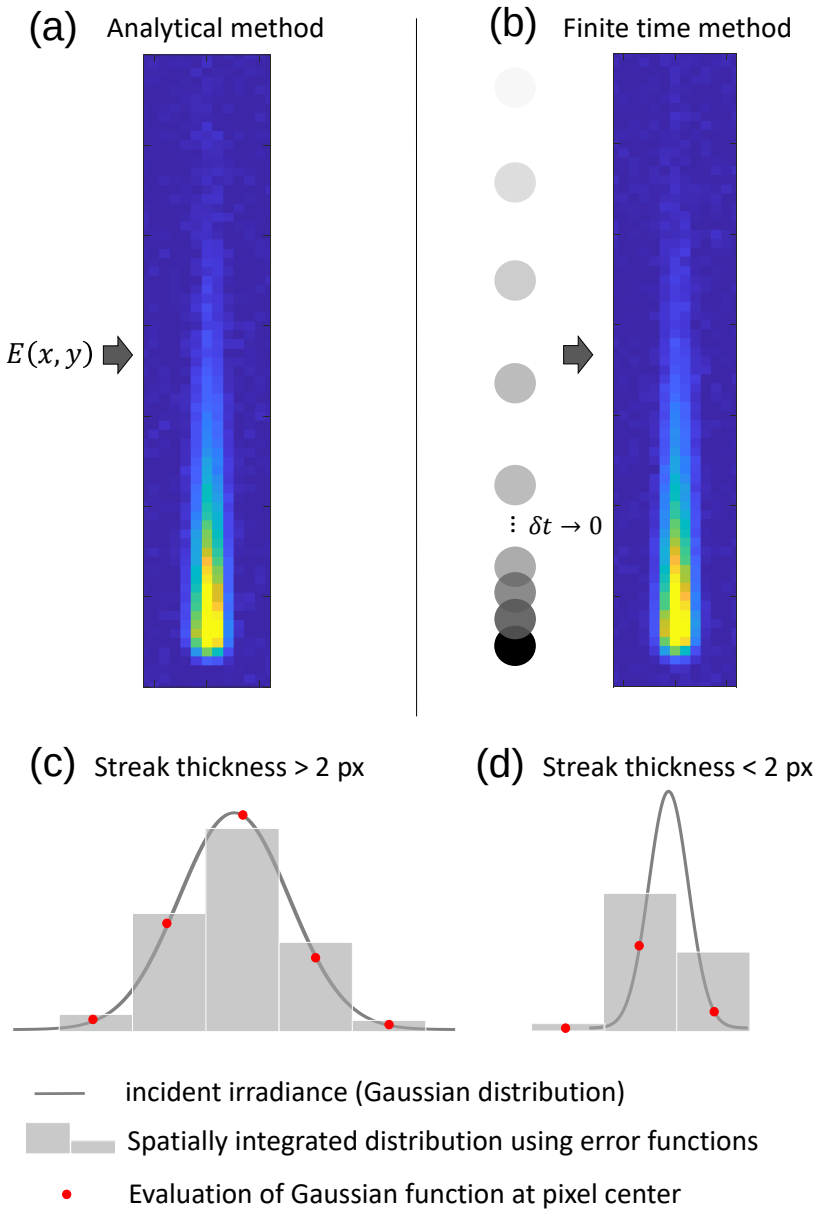

Figure 5: An example phosphor streak generated by the (a) analytical method using Eq. (7), and (b) finite time method with the same inputs. Comparison of spatial intensity distributions along one direction for the incident Gaussian irradiance (grey profile), spatially integrated pixel counts using the errorfunction (grey bars) and Gaussian distribution estimated at pixel center (red dots); (c) for a wide particle image across multiple pixels where both methods produce similar result and (d) for a small particle image. In the latter case, the analytical method (red dots) may not truly reproduce the image recorded by a camera (bars), and a misalignment error will be present relative to the true unpixelated intensity profile (grey line).

was used in order to investigating the lowest detectable velocity as well as the flow streamline effects.

3. Flow measurement results

3.1. Velocity measurements in a low speed (< 20 cm/s) liquid flow using GOS:Tb^{3+} particles

Figure 6 shows a series of velocity fields measured by GOS:Tb^{3+} particle in the stirred cuvette. Each single shot contains more than 2000 individual vectors (magnitude shown by the vector colour). Thanks to the high vector density in this demonstration, spurious vectors which deviate more than 2.5 times of the standard deviation from the local mean, as well as those removed due to unsuccessful fits (hit the bounds), were simply replaced by the median value of neighbouring 9 vectors, similar to PIV post-processing. For this high streak image density case, the replaced or inserted vectors comprised about 8-10% of the total streak number on each single shot, due to clusters in which streaks were too close to be isolated. Figure 6 clearly shows the evolution of vortices, particularly, the formation and disappearance (perhaps moving towards out-of-plane) of an eddy in the bottom left corner. The largest and smallest velocity vector in this cuvette flow is about 17 cm/s and 1 cm/s, respectively, with an average vector density ∼0.004 vector per pixel in these instantaneous vector fields. These results demonstrate the utility of this method/phosphor combination in low velocity flows, which covers applications in thermal convection studies.

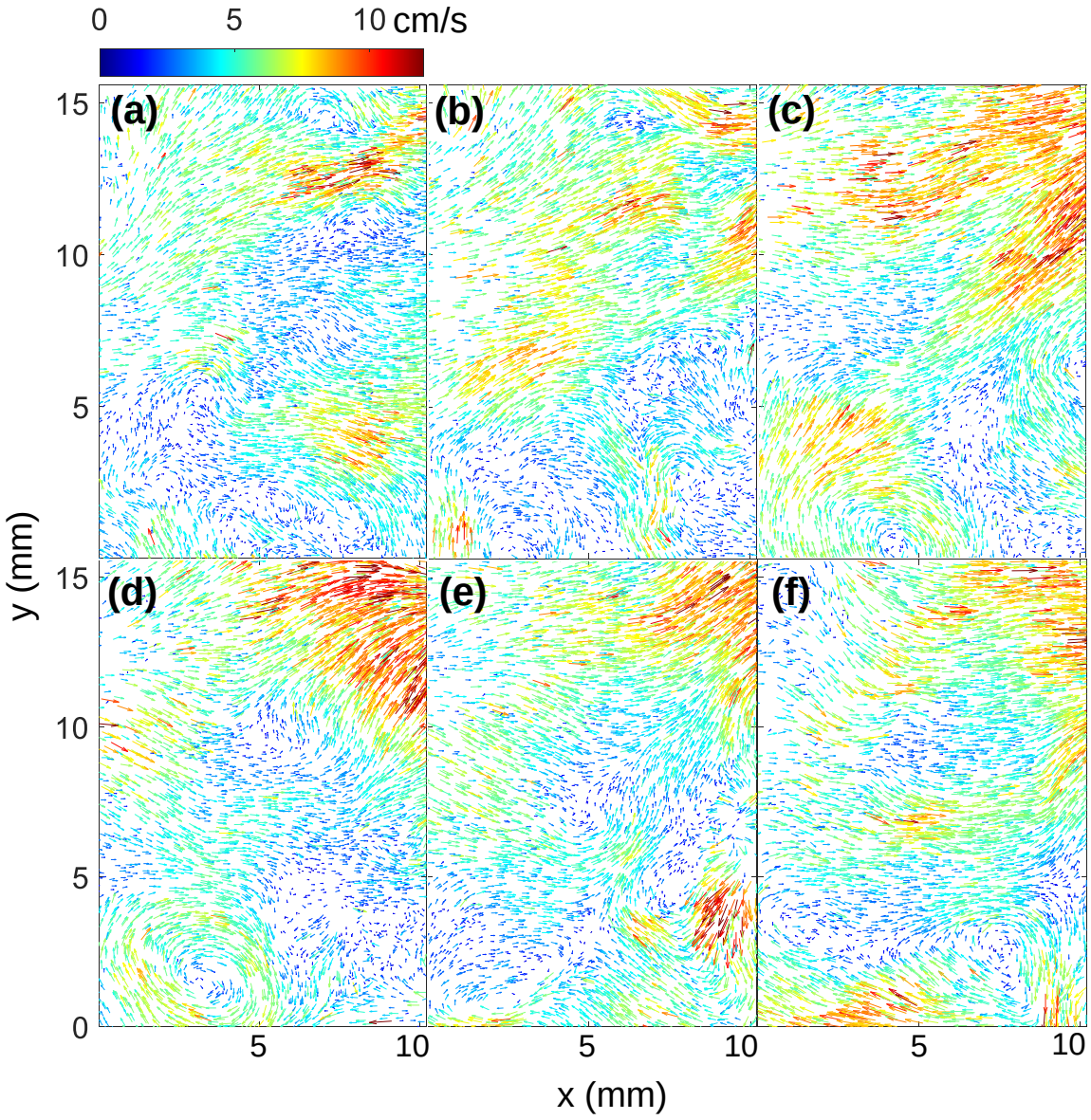

Figure 6: (a)-(f) Six consecutive single shots of the velocity field measured by the streaks. (d) corresponds to the raw image shown in Figure 4(a) where an eddy can be observed in the bottom left corner.

3.2. Velocity measurements incompressible (Ma∼0.02) air jet using SMP:Sn^{2+} particles

In this subsection, the low velocity jet data recorded with SMP:Sn^{2+} and described in our previous letter [1] were reprocessed with the new image dilation method. This is to illustrate in this paper an intermediate velocity range and to validate the new image dilation technique against the PIV measurements of that study.

Figure 7(a) and (b) show the same instantaneous field of an air jet at a ∼3.7 m/s bulk velocity (Re = 2400), using the image dilation and the previous rectangular window segmentation method, respectively. For this low ~~seeding density~~ particle streak density case, the image dilation method results in 9% more vectors ~~than that~~ in comparison to the fixed window method, indicating a higher successful fitting rate even at low seeding densities. Figure 7(c) compares the mean axial velocity profiles produced by the two segmentation methods, as well as the reference profile obtained by simultaneous PIV. The profiles with the image dilation method show an excellent agreement with PIV results. In the shear layer, the new dilation segmentation method achieved better agreement with the PIV profile than the window-based segmentation method. In addition, the rms velocity, which mainly originates from random error of the PSV technique is lower with the new technique in the whole profile, with 78% in the core and 96% in the shear layer.

3.3. Turbulent jet measurements by BAM:Eu^{2+}

Figure 8(a) presents a single-shot raw image of a 10 mm inner diameter, Re = 55000, turbulent air jet measured with BAM:Eu^{2+} particles. In highly turbulent gaseous flows, keeping uniform seeding is a well known challenge. As can be observed from Figure 8(a), large streak clusters consisting of dozens of streaks were formed

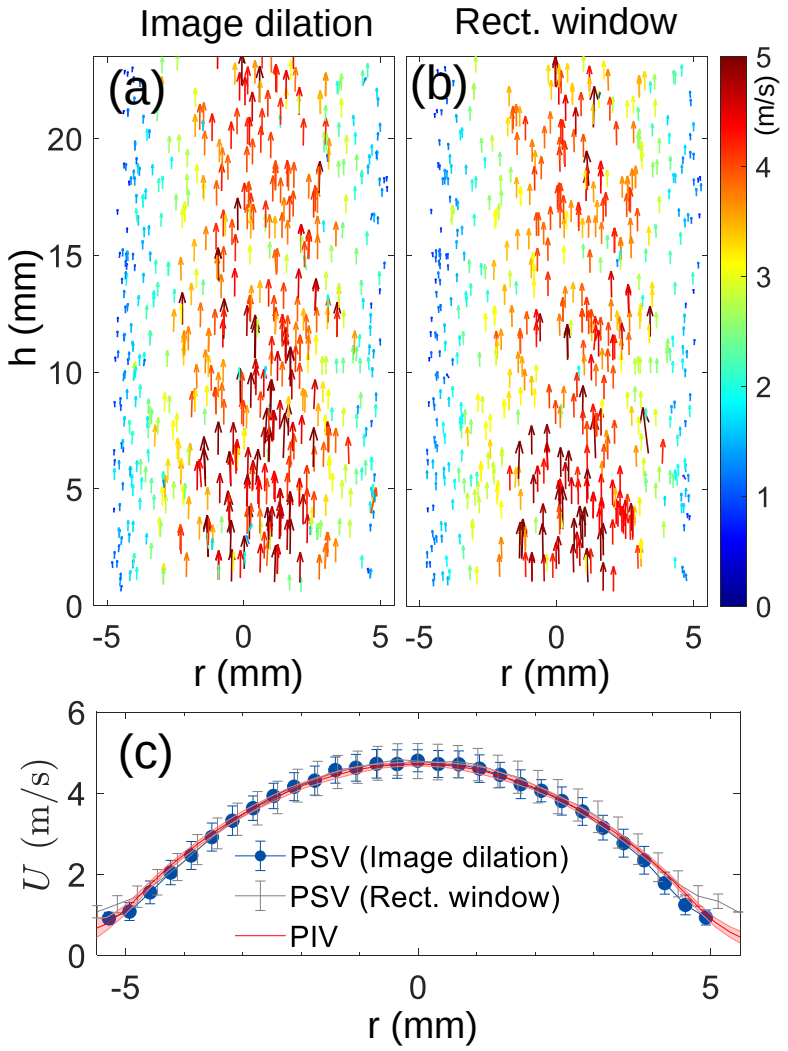

Figure 7: An example instantaneous velocity field of an Re = 2400 air jet measured by SMP:Sn^{2+} using (a) the image dilation method, and (b) the previous window-based segmentation method [1]. (c) A comparison of axial velocity profiles (h < 5 mm) obtained by the two segmentation methods, and simultaneous PIV results. The error bars and shaded area are RMS velocities for PSV and PIV, respectively.

due to the high ~~seeding density~~ particle streak density, while some regions inside the jet had few particles. Figure 8(b) shows the velocity field extracted from the corresponding snapshot. Comparing with the apparent number of particles shown in Figure 8(a), the number of vectors successfully extracted is relatively low, indicating some too-close streaks were not successfully identified. Although theoretically the segmentation method we proposed here can deal ~~an~~ up to 0.01 streak per pixel (see Subsection 2.6), yet, such estimation was made based on a uniformly dispersed particle field. When computing turbulent statistics from the instantaneous velocity fields; we observed a surprisingly high rms velocity at 45% of the mean. As shown later, turbulence intensities for such jet is expected to be below 5%. We interpreted the larger observed fluctuations to the fact that the emission lifetime of BAM:Eu^{2+} may be sensitive to laser fluence. Previous studies have shown that the fluence indeed influences the emission spectrum [18, 21], hence may also have an effect on the lifetime. Particles at various position within the light thickness can experience different laser fluences. To limit the sampling to a subregion of the light sheet where the laser fluence is more uniform, we decide to exploit the shallow depth of field of the imaging system. By filtering the data by streak size delta (σ), we can limit the sampling to particles within a smaller range of out-of-plane positions.

Only sharply focused streak images with a size constant $\sigma < 0.7$ px (estimated effective depth of field < 60 μm) were used to calculate the statistics and the accumulated vector field shown in Figure 8(c). By this mean, the rms velocity dropped to only 10%. However this naturally leads to a lower vector density everywhere in the image (17% of the original density). The reduction was particularly dramatic below $h = 1D$, possibly due to a slight tilt of the light sheet with respect to the focus plane of the imaging system. The effect of laser fluence on phosphor-PSV measurements for fluence-sensitive phosphors will be explored in more detail in the

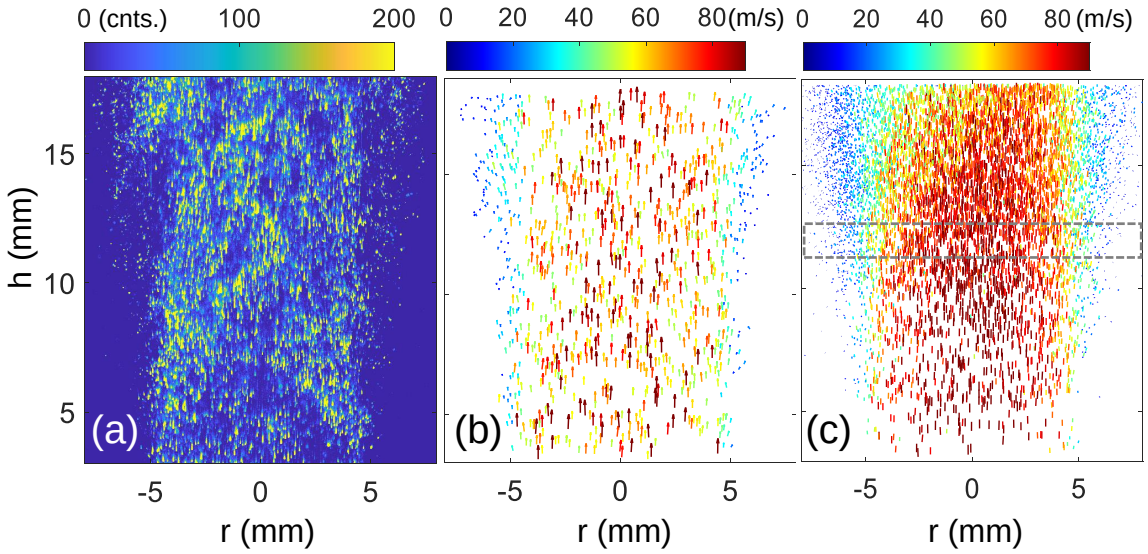

Figure 8: (a) A single-shot raw image of the Re = 55000 air jet flow seeded with BAM:Eu^{2+} particles; (b) the velocity field measured by the BAM:Eu^{2+} emission streaks in (a); (c) accumulated vector field of the turbulent jet, conditioned by $\sigma < 0.7$ px to keep select particle experiencing a similar range of laser fluence.

future. To minimise fluence variation for such fluence-sensitive phosphor materials, holographic beam homogeniser should be used.

Statistics were derived from 600 single-shot vector fields conditioned by $\sigma < 0.7$ px. Figure 9 shows the mean and rms velocity profiles extracted from accumulated vector fields at $h = 1.2D$, marked by the dashed rectangle in Figure 8(c). The mean profiles were compared with PIV, which was conducted separately with the same batch of phosphor particles. A comparison with data from an early study [22] of a similar round air jet of a similar Reynolds number Re = 51000 at the same height obtained by hot-wire anemometry (HWA) is also presented. The turbulent pipe flow is expected to be fully developed in both experiments. Since in that study the Reynolds number was estimated based on the mean axial velocity at the centre line, the Re = 55000 for our case was calculated the same way for consistency. The

results are shown in Figure 9. The mean profiles obtained by PSV, PIV and HWA (the peak of HWA profile normalized to match $U_0 = 85$ m/s) agree well within $\pm 0.4D$, ranging from 70-85 m/s in this region. Beyond this, the PIV results are slightly higher, likely attributed to both a deterioration of cross-correlation quality caused by the entrainment of unseeded co-flow, which occasionally produces some nonphysically large vectors, and an insufficient spatial resolution to resolve the steep velocity gradient across the shear layer. By observing the rms profiles, we can see that phosphor PSV also exhibit peaks in the shear region of the jet, demonstrating the utility of this method/phosphor combination for the study of subsonic compressible flows. Again, the rms of the PIV results significantly biased to a higher value due to strong entrainment of the unseeded ambient flow beyond $r = \pm 0.4D$. In the jet core region, however, the rms axial velocity $u'/U_0 = 9\%$ measured by phosphor-PSV ~~of 9%~~ is higher than 4% in the HWA measurements ~~of 4%~~ [22]. This is due to a contribution of the phosphor PSV random uncertainty of about ~8% precision of the technique, which will be further discussed in Subsection 4.2.

To determine the accuracy of the technique in this velocity range, two other flow rates were tested using the same jet. The axial velocities measured at $h = 1.2D$ are presented in Figure 10. Within the 26-85 m/s velocity range, the mean velocities obtained by PSV are consistent with those given by PIV, and the rms velocity counts for 8-12%, contributed by both turbulent fluctuation and precision of the PSV technique, as will be further analysed in the following section.

4. Uncertainty analysis using synthetic streak data

In this section, the uncertainty and dynamic range of phosphor particle streak velocimetry are investigated. Synthetic streaks are generated and compared to experimental streaks.

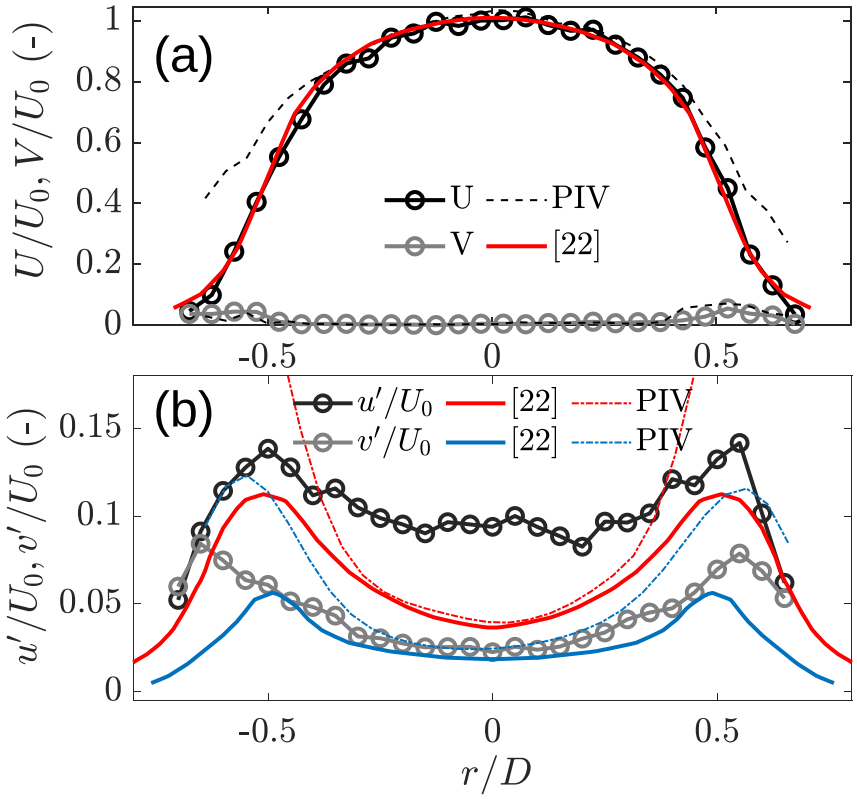

Figure 9: (a) Normalized mean and (b) rms velocity profiles extracted at $h = 1.2D$ measured by BAM:Eu^{2+} PSV, PIV, and hot-wire data in an open air jet of a similar Reynolds number Re = 51000 from [22] also at $1.2D$ (by interpolating $h = 1D$ and $2D$ profiles linearly). Data from [22] was normalized to match the peak axial velocity.

4.1. SNR, particle size constant, and spatial resolution

To investigate the effect of SNR, particle size constant, and spatial resolution on the calculated velocity, virtual phosphor streaks were simulated under various conditions (2000 streaks for each condition), and then processed by the fitting approach. Here, we applied a same level random readout noise to all pixels. The SNR was defined as the peak intensity over the standard deviation of the background noise, consistent with our previous letter). The mean and rms error in the velocity measurements are presented in Figure 11. According to Figure 11(a), for a SNR

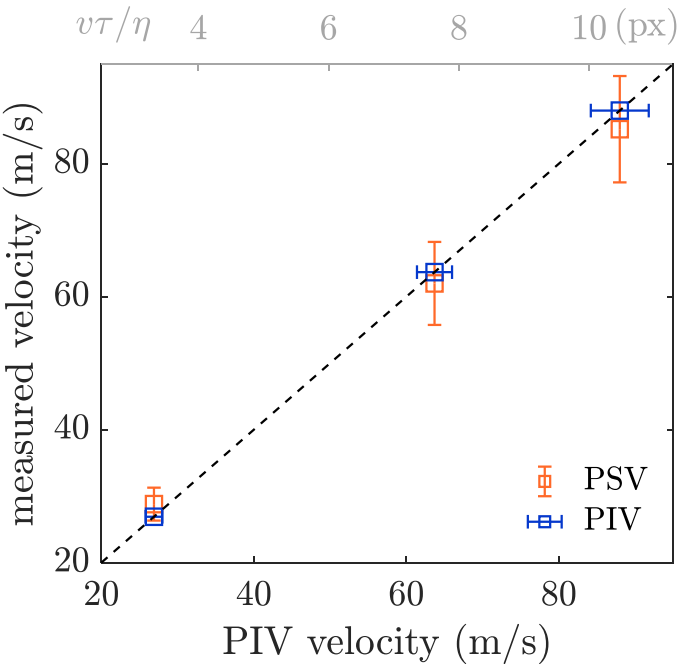

Figure 10: Comparisons of centre-line axial velocity at $h = 1.2D$ obtained by PIV and the value measured by PSV for different flow rates. The rms velocities are marked by the error bars.

higher than 20, the measured mean velocity shows negligible bias, and the precision is better than 3%. For a SNR as low as 5, the mean bias still counts less than 2%, although the precision is compromised to about 13%. Figure 11(b) shows the effect of the particle size constant σ (streak thickness $= 4\sigma$) on the velocity measurements. Unless the streak size constant is below ($\sigma < 0.3$ px) we did not observed an increase in bias error in the range of 0.3 to 2 pixels. ~~as observed in the case of conventional PIV/PTV, typically caused by so-called pixel locking [23] in PIV/PTV. This is because the streak length in PSV is de-correlated from the particle size constant σ, even a small σ can produce a long streak depending on the velocity, while for PIV the σ determines the sub-pixel positioning accuracy and ultimately the displacement accuracy. Hence, a small σ may cause a positioning error but does not influence the~~

~~calculated velocity in PSV.~~ However for overly-thin streak ($\sigma < 0.3$ px), a bias error appears, similar to the pixel locking effect in PTV [23]. Regarding the precision (rms error), it slowly increases as the size constant decreases to $\sigma = 0.3$ px, and then sharply increases. To better understand the errors for small particle images, we investigated the effect of the particle image center position with respect to the pixel area. We simulated $\sigma = 0.2$ px streaks at different subpixel positions along the lateral direction x, from 0 (particle centre projects onto the edge of a pixel) to 0.5 px (particle centre projects onto the centre of a pixel). A clear trend in the errors against the particle image center to pixel center distance is observed, as shown in Figure 11(c). When the particle image center and the pixel center match, the streak has only one intense column of pixels ($x_{0,\text{sub}} = 0.5$ px) and this leads to a maximum systematic error as well as a maximum random error. This is due to two possible reasons: (1) singularity caused by this ill-posed problem (apply a 2D fitting to only 1 line of pixels); and (2) the valid number of pixels (data points) for the fitting is reduced by half comparing with the $x_{0,\text{sub}} = 0$ px case. Between $0 < x_{0,\text{sub}} < 0.5$ px, similar differences between intensity distribution from spatially integrated and directly evaluated streak expressions as those shown in figure 5(d) will be present (the difference between the red dots and the grey bars), which contributes to errors in the fitting result. Fortunately, due to lens aberrations in widely opened luminescence imaging objectives and a shallow depth of field, streaks with a σ smaller than 0.4 px only takes 1.5% of the total streak number. However, if using cameras with a large pixel pitch size, e.g. high-speed CMOS cameras to acquire the streak images, streaks with $\sigma < 0.3$ px may occur more frequently. As σ approaches to zero, the exponential part in Eq. (2) becomes a Dirac function. Therefore, for overly-thin streaks that only contain one line of pixels, a 1D model that directly correlates the signal decay and particle displacement should work better. The effect of the fill ratio

of the sensor array, as well as the effect of aberration on phosphor streak velocimetry accuracy should be also investigated using virtual streaks in the future.

As discussed in our previous work [1], the upper limit of velocity dynamic range is limited by the signal-to-noise ratio, as longer streaks usually have lower signal-to-noise ratio. The lower limit, however, is determined by the spatial resolution of the image acquisition system. Figure 11(d) shows the theoretical minimum displacement that can be resolved by the fitting method. When the displacement $v\tau/\eta$ (v here is in m/s; η represents the pixel resolution) projected on the sensor is less than 1 px, a large mean and rms relative error is observed. With the presence of noise in the particle image, the fitting can no longer determine the actual intensity profile based on the discrete information from so few pixels. This is similar to PTV, in which the Gaussian estimator cannot achieve subpixel accuracy for a particle image with a diameter less than 1 px (pixel locking). In practice, a particle diameter larger than 3 px has been suggested for PTV to minimize the effect of pixel locking in a previous study [24]. A similar value could be applied as the minimum streak length for a robust fit, as will be verified in the following subsection.

4.2. Dynamic range

Following a similar numerical approach, we use virtual streaks to predict the dynamic range of phosphors and compare with the experimental result. First, we use the parameters extracted from the SMP:Sn^{2+} data in the air jets to demonstrate such a simulation. Unlike the above simulations regarding SNR etc., here however, we aim at assessing the noise level accurately. For that, the real distribution in total streak intensity (sum of pixel intensities over a streak) obtained in measurements was used, shown in Figure 12. A median intensity of 6800 counts was obtained for SMP:Sn^{2+}. The readout noise level for the sCMOS camera of 5.5 counts under the

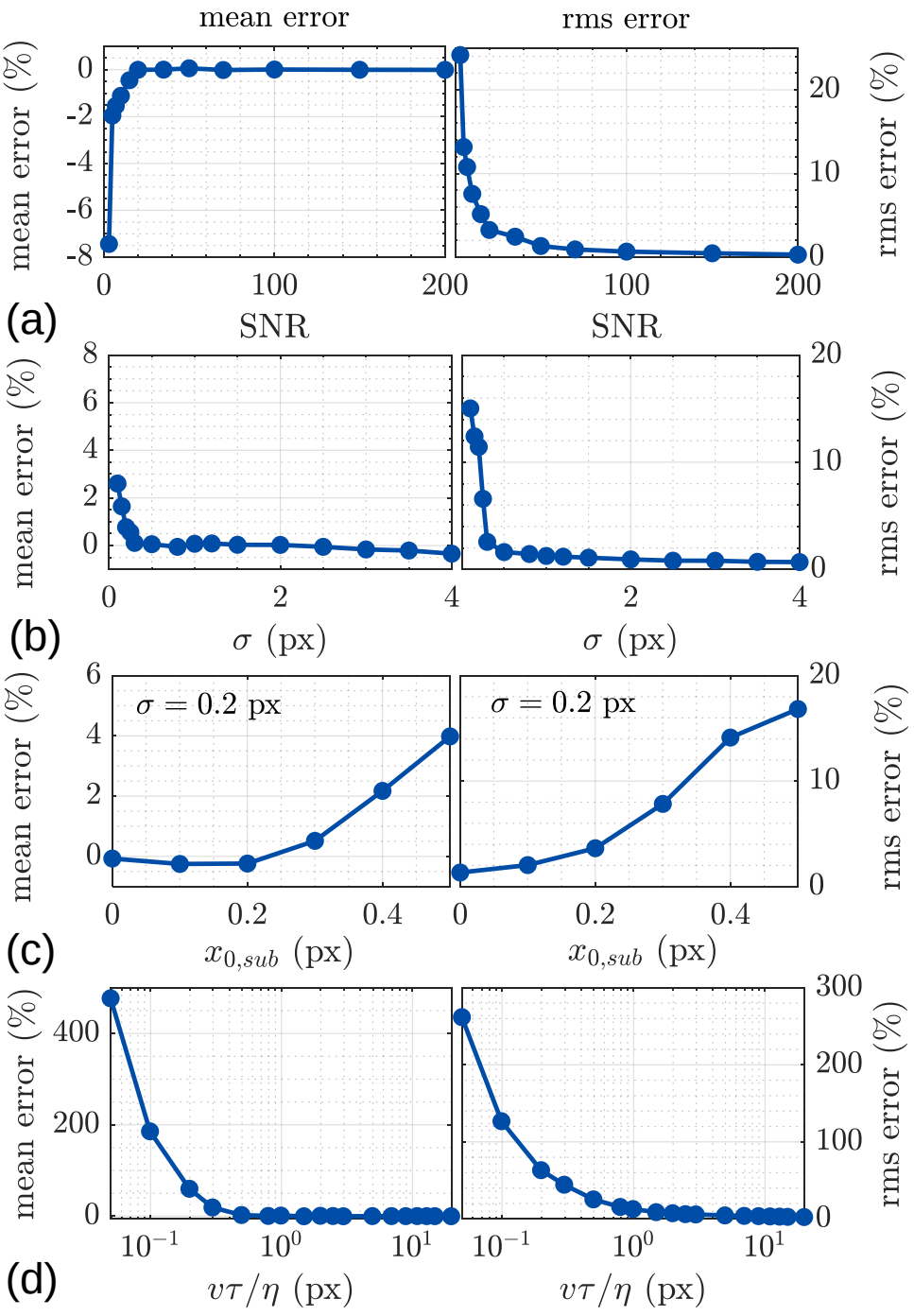

Figure 11: Mean and rms error (%) in velocity extraction as a function of (a) SNR, (b) particle size constant σ, (c) subpixel position $x_{0,\mathrm{sub}}$ while $\sigma = 0.2$ px, and (d) displacement $v\tau/\eta$, where η is the pixel resolution. The otherwise unchanged parameters are SNR = 20, $\sigma = 1$ px, $v\tau/\eta = 20$ px and a random $x_{0,\mathrm{sub}}$ between 0 and 1.

rolling shutter mode was considered, and a mean background of 50 counts was added to the virtual images. The shot noise in each pixel follows a normal distribution bounded by a standard deviation equals to the root mean square of the local pixel intensity. The overall noise in each pixel is then $\delta=(\delta^2_{\text{readout}} + \delta^2_{\text{shot}})^{1/2}$. Here, the SNR of a streak is defined as the ratio of peak intensity over δ at this location. This gives a mean SNR = 5.4 for tin-phosphor particle images in a 20 m/s flow and 37 for 0.1 m/s. Figure 13 shows the comparison of numerical predictions and experimental results. We define the dynamic range where both the mean and rms errors remain below 10%. The simulation gives a dynamic range of $v\tau/\eta$ = 0.8-22 px (0.3-8.4 m/s), slightly wider than the 4-20 px (1.5-7.6 m/s) range estimated from the experiment.

For $v\tau/\eta < 5$ px, the relative rms errors are under-predicted by the virtual streaks, as shown in Figure 13(b). These differences can be attributed to the fact that real streak images are non-ideal due to aberration or other effects caused by the collection angle, filter quality, etc. The contribution of image defects as a function of pixel displacement was estimated by subtracting the contribution of the virtual streak error to the measured error in Figure 13(b). The data were fitted by an exponential function which is also plotted in figure Figure 13(b). For such a low velocity relative to the long decay time of the phosphor, the number of pixels used for fitting is significantly reduced. Hence, any defect in a very short streak image could strongly bias the fitting result. For long streaks, however, defects in streak images are much less influential on the calculated velocity and thus the uncertainty analysis by virtual streaks is much closer to real experimental level comparing with that for PIV. From Figure 13(b), we see that the image defects are larger than the random errors at a displacement of 5 px, and therefore we can estimate the minimum number of pixels to reduce fitting error from defects in a streak image: 5 px $\times$ 3 (3τ so the intensity drops to $1/e^3 \approx 0.05$) $\times$ 6 px (streak apparent width 6σ) $\times$ 0.5 (triangle) + semicircle

head = 50 px.

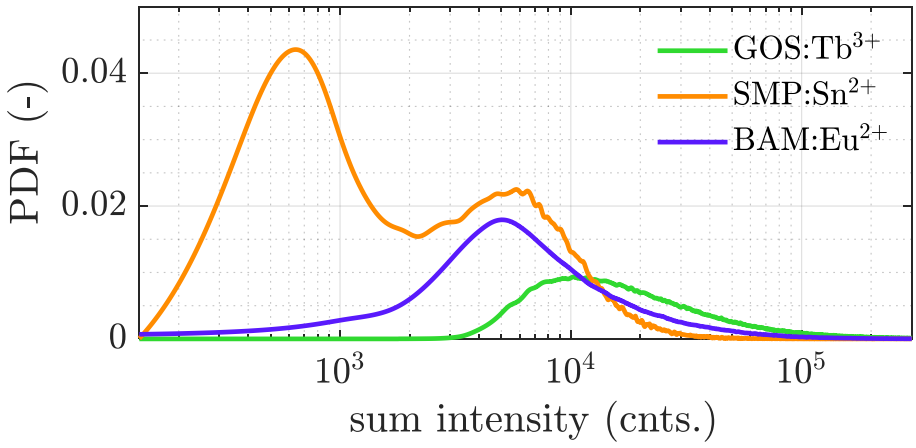

Figure 12: PDFs of sum intensity for the three phosphors obtained from the streak data. The median sum intensity is 6800, 14000, and 35000 counts for SMP:Sn^{2+}, BAM:Eu^{2+}, and GOS:Tb^{3+}, respectively.

Phosphors with a higher emission intensity can extend the maximum detectable displacement. Using the simulation approach demonstrated above, Figure 13(c) and (d) present the rms errors as a function of the displacement and the absolute velocity for the three phosphors, according to their emission intensity distribution shown in Figure 12. The experimental data for SMP:Sn^{2+} and BAM:Eu^{2+} are plotted in Figure 13(d) for comparison. The estimated rms error due to image defects has also been added to the curves in order to present a more realistic estimation on the dynamic range as in experiments. Following the same 10% criterion (marked by the gray dotted line in the figure), the theoretical dynamic range is estimated as $v\tau/\eta$ = 3.5-730 px (0.045-9.5 m/s) for GOS:Tb^{3+}, and 3.5-140 px (28-1115 m/s) for BAM:Eu^{2+}, although measurements at such high velocities would be very challenging, in particular due to high particle Stokes number across shocks. With the image defects error added to the curves, both ends of the dynamic range are controlled by the 10% rms error rather than by the mean bias. Note that the 3.5 px minimum

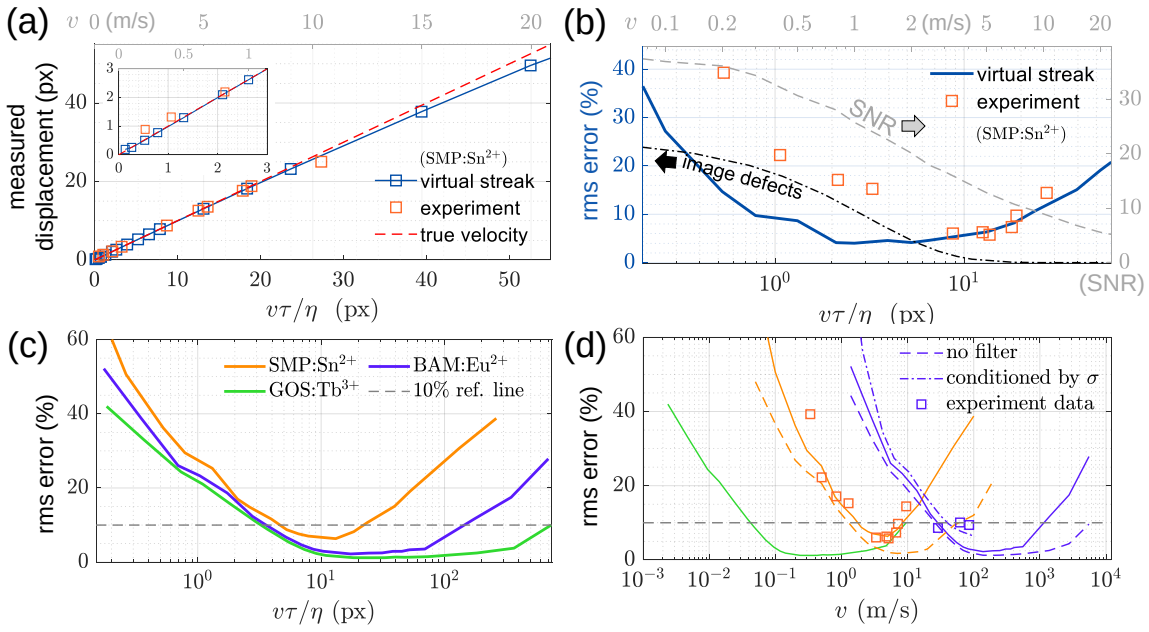

Figure 13: (a) Numerical prediction and experimental data on the accuracy of SMP:Sn^{2+}-based phosphor-PSV over a range of displacements $v\tau/\eta$ (in pixels); (b) measurement precision as a function of mean displacement. The corresponding SNR for each velocity case is also plotted as the gray dashed line. The rms error due to image defects for streaks below 10 px are estimated from the experimental data (fit by an exponential model and plotted as black dotted line in (b)). The values on top axis is the corresponding velocity (m/s); Mean and rms error predicted for the three phosphors as a function of (c) displacement $v\tau/\eta$ and (d) velocity v. The jet data obtained in the experiments are also plotted in (d) for comparison. The estimated rms error due to image defects has been added to the curves in (c) and (d). The gray dashed line in (c) and (d) marks the 10% rms error which defines the velocity dynamic range.

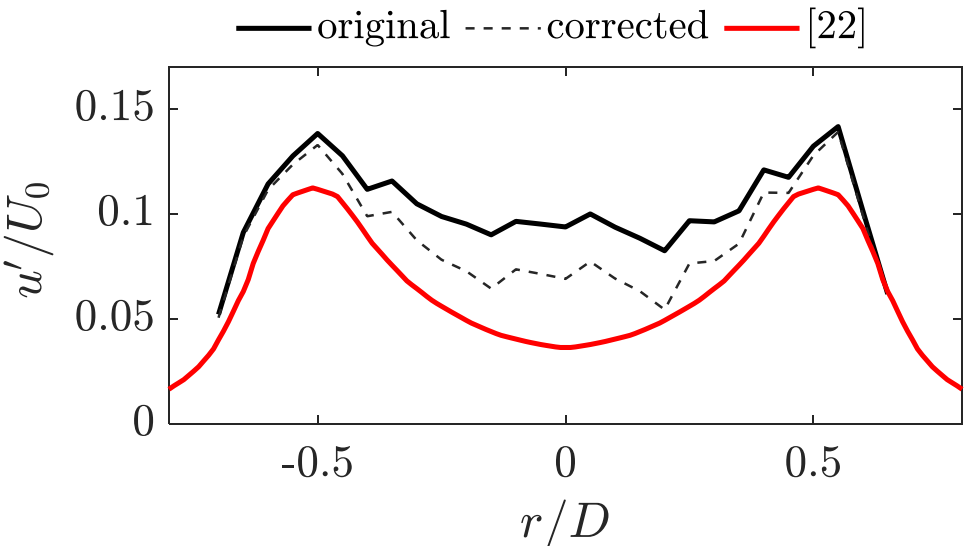

Figure 14: The original and the corrected axial velocity profile of the Re = 55000 air jet. The profile obtained by HWA [22] is also plotted for reference.

displacement coincides with the minimum particle size (3 px) used to avoid the pixel locking effect in practical PTV measurements as suggested by [24], and is probably a universal criterion for algorithms based on 2D Gaussian fits, regardless the phosphor used. Estimations were also made for cases where the whole luminescence band is collected (convoluted with quantum efficiency curve of the sCMOS camera) without using any optical filters, as they were far from being optimal for velocimetry purpose. It was found that under this conditions the theoretical maximum displacement for SMP:Sn^{2+} and BAM:Eu^{2+} would be further extended to 160 px (60.9 m/s) and 740 px (5895 m/s). However, before entering into the supersonic velocity range, streak curvature effects in a flow with vorticity may also occur, which is discussed in Section 6.

To estimate the random uncertainty in the turbulent air jet measurements, we also needed to consider the effect of the conditioning of the particle image size constant

on the intensity distribution. For this, the sum intensity distribution of the filtered streaks was computed, which was found to cover lower intensity range compared to the unfiltered data (the median value dropped to around 7000 counts). We presume that this is due to a shift between the focusing plane of the imaging system and the high intensity region of the light sheet, so that the focusing plane is located in a lower intensity region of the light sheet. The rms error predicted for the conditioned streaks ($\sigma < 0.7$ px) is also shown in Figure 13(d) as the dash-dotted line. We used this error prediction to determine and subtract the role of random measurement error on the turbulent fluctuation profile of the Re = 55000 air jet using $u_{\text{corrected}} = u_{\text{original}}(1 - \epsilon_{\text{rms}}^2)^{1/2}$, where ϵ_{rms} is the rms error. The corrected profile is presented in Figure 14. Precision of the measurements in the core region is estimated as 6.9%, thus the true velocity fluctuation is further reduced to 6-7%. The residual 2% rms velocity comparing with the profile measured by HWA [22] may be attributed to the segmentation error due to severely overlapped streaks and residual laser fluence variation within the depth of field.

Apart from choosing the right phosphor, or τ, to suit the flow velocity, the other adjustable parameter in $v\tau/\eta$ is the projected spatial resolution η. Since most camera lenses have an adjustable focusing distance, theoretically the dynamic range can be shifted towards a higher velocity range by reducing the magnification of the imaging system, for example by moving the camera further away from the object. However, at fixed f number, the total streak intensity will decrease with a decrease in the magnification, which leads to a weaker streak with a lower SNR. As a result, the actual range will be made narrower with demagnification.

4.3. R^2 as an estimation of uncertainty

The goodness of the fit can also provide information on uncertainty. This is particularly useful when a wide range of SNRs are presented in the experiment due to a wide particle size distribution of the phosphor powder. We define an expression similar to R^2 in statistics:

$$R^2 = 1 - \frac{\sum(I_i - I_{\text{fit,i}})^2}{\sum(I_i - \bar{I})^2} \tag{11}$$

where I_i denotes the intensity of the i^{th} pixel in a streak collected by the camera, $I_{\text{fit,i}}$ is the corresponding fitting result, and $\bar{I}$ is the average intensity of the streak. This expression can reasonably reflect the quality of the fit. Figure 15(a) shows a correlation between R^2 and the measurement uncertainty for a displacement $v\tau/\eta$ = 8 px. Virtual streaks with various SNRs ranging from 4-100 were simulated and processed by least square fitting. The R^2 value of each fit is plotted against the x axis, whereas the error in the velocity measurement given by that fit is plotted against the y axis. The black curve shows the corresponding uncertainty envelope at 95% confidence. The uncertainty in each velocity vector can be estimated directly from this plot by calculating the robustness of the fit. Figure 15(b) shows the uncertainty envelopes calculated for different displacement $v\tau/\eta$. Above 2.5 px the 95% confidence bound gradually converges due to a sufficient number of effective pixels to accurately determine R^2, where the goodness of the fit can reasonably represent the uncertainty in the velocity measurement.

We again examine the laminar jet data presented in Subsection 3.2 to calculate the R^2 for each streak and correlate the goodness of fit with the difference between the retrieved velocity and the local mean. Results are plotted in Figure 15(c). According to the scatter plot, 80% of the fitting is with a R^2 larger than 0.6, and the

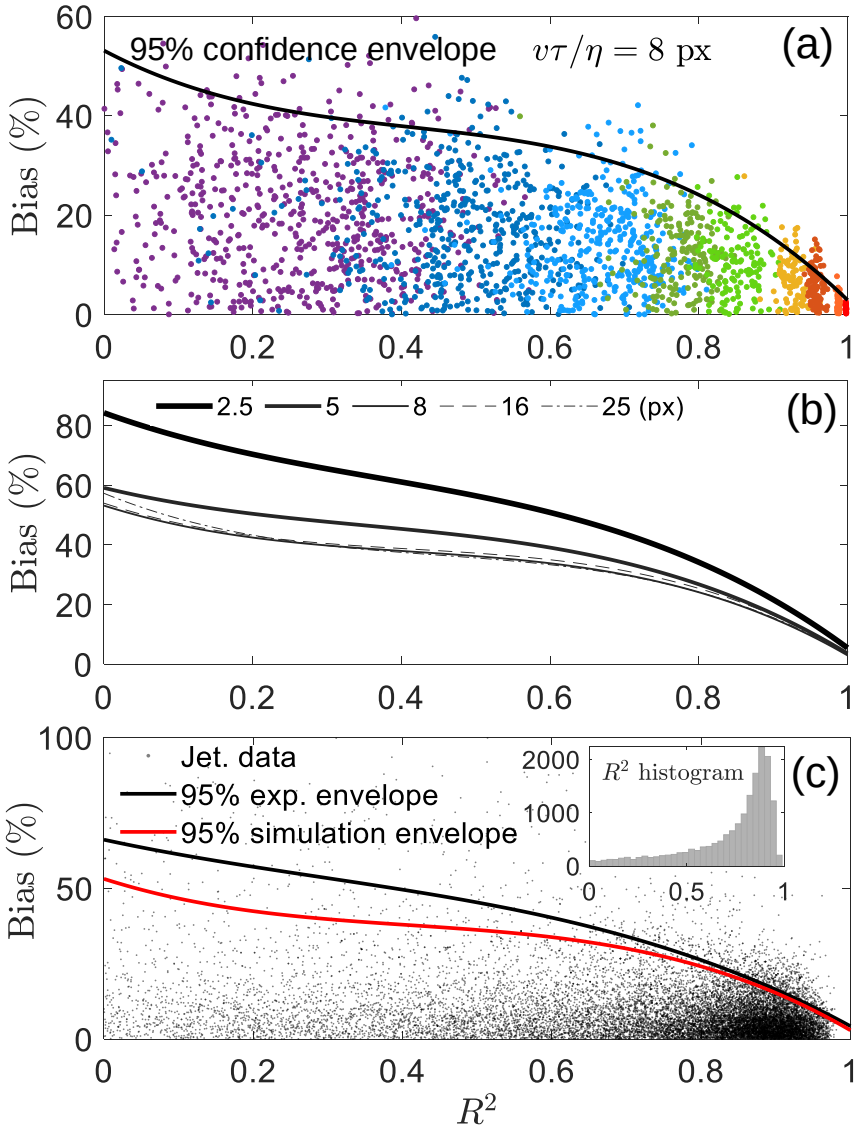

Figure 15: (a) The scatter points are virtual streaks synthesized based on different SNRs (colours from left to right: SNR = 4, 5, 6.5, 8, 10, 15, 20, 40, 100). The y axis shows the relative error in the retrieved velocity, and x axis is the corresponding R^2 value for the fitting. The black curve shows the envelope of uncertainty at 95% confidence. (b) The uncertainty envelope calculated at different displacements.(c) Experimental jet data with SMP:Sn^{2+} (core region of the jet shown in Figure 7, $v\tau/\eta \approx 12$ px), the 95% envelope for the experimental data, and the predicted uncertainty envelope. The mini-figure shows the histogram of R^2 calculated from the jet data.

experimental envelope shows a satisfactory agreement with the uncertainty envelope predicted, especially in large R^2 regime where sufficient data points converge the statistics.

To demonstrate the idea of performing error analysis based on the goodness of fit, we estimated the rms error for the BAM jet measurement at 85 m/s using the R^2 without conducting simulations: the mean R^2 in the measured data (conditioned by $\sigma < 0.7$ px) was 0.875; This corresponds to a 19.2% random error with 95% confidence by looking up to the converged envelope in Figure 15(b). Assuming the random bias in individual streaks obeys a normal distribution, the rms error then contributes to approximately 6.4% (1/3 of 19.2%) in the overall 9% rms velocity. This is very close to the predicted precision (6.9%) using the BAM:Eu^{2+} intensity distribution shown in Figure 13(d). Hence, the average R^2 can be used as a universal measure to evaluate the precision of the measurements regardless the type of phosphor used, by referring to the envelopes plotted in Figure 15(b) directly.

The analyses in this section suggest each type of phosphors has its own applicable velocity range, limited by both the minimum SNR and minimum number of pixels for a robust fit. The magnitude of the dynamic range depends on the emission intensity of the phosphor used. Using a parameter R^2 representing the goodness of the fit, the uncertainty in each velocity vector can be evaluated.

5. Flows with out-of-plane motion

Although this paper focuses on 2D phosphor-PSV for two-component velocity measurements, it is still necessary to discuss the effect of out-of-plane motion of particles which is unavoidable in most turbulent flows. In all above-mentioned experimental cases, the flow motion is primarily in-plane. It is well known that the

valid detection probability of the correlation peak for PIV degrades when the number of missing/emerging particles on the second frame becomes significant due to out-of-plane motion. In PTV, missing particles would affect the particle searching algorithm, and lead to incorrect matches. Based on these points, it was decided to investigate the effects of out-of-plane motion on phosphor-PSV. For this purpose, we conducted PSV in an air jet with $v_z/v_y = 10\%$ and 40% out-of-plane motion, by introducing a 5.6° and a 22° inclination angle (towards the camera) to the jet, respectively. SMP:Sn^{2+} particles were used as the tracer. The mean axial velocity of the jet in the core region is 4.8 m/s, measured in separate experiments by a normal PIV with no inclination. We processed all images from the two cases in the same way as for jets with no inclination, and results are presented in Figure 16. The mean velocity averaged spatially in the region highlighted in the figure is 4.6 m/s and 4.4 m/s for the two cases, respectively, which shows a satisfactory agreement with their theoretical counterpart 4.77 m/s and 4.45 m/s, derived from the velocity profile of the upright jet. Note that the in-plane vectors extracted from the projection of a 3D streak may still be affected by perspective error which is caused by a varying magnification factor across the z-plane [25]. For example, in the 40% out-of-plane motion case, the perspective error could cause an up to 8% bias in the in-plane velocity at the corner of the image.

Figure 17 shows two sample PSV images for the two cases with out-of-plane motion. The enlarged view of two example streaks are also displayed on the right side of the figure. 10% out-of-plane motion seems to have little effect on the streaks, whereas for the 40% case, the streak images appear to be thicker and out of focus. Figure 18 shows histograms of streak size constant for the jet flow at 0°, 5.6°, and 22° inclination angles. The peak of the histograms shows a clear shift to a larger σ as the out-of-plane component of the velocity increases, confirming the defocusing

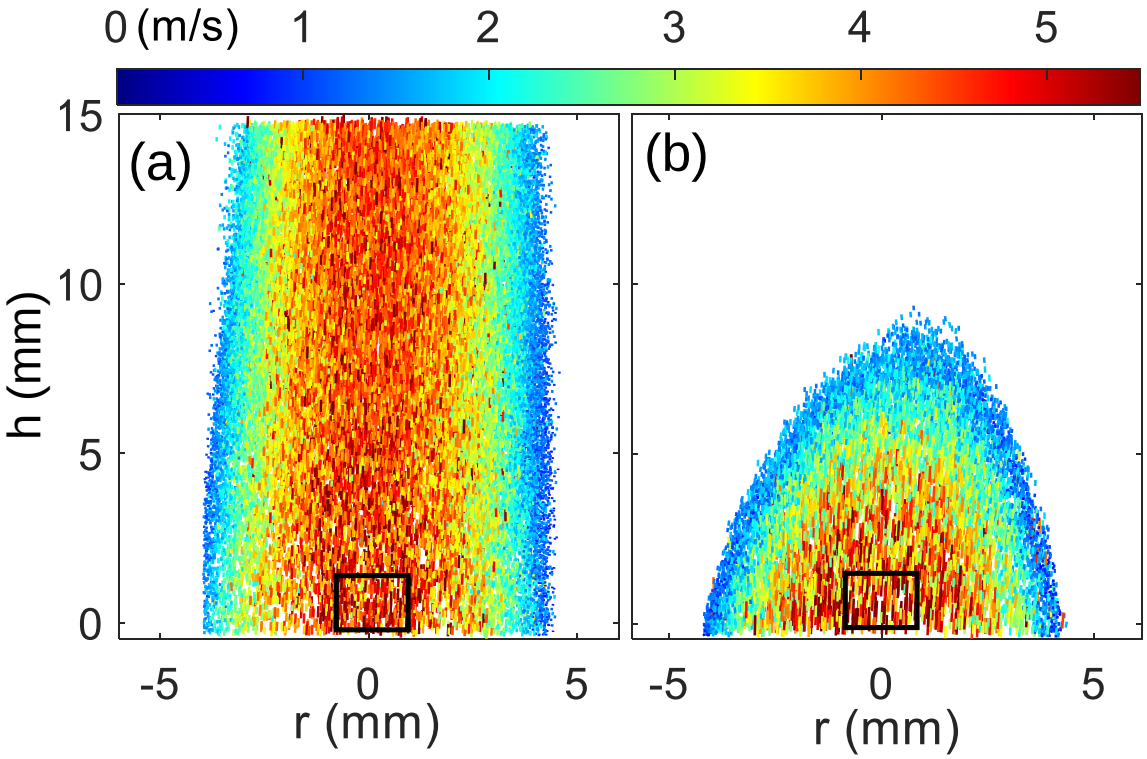

Figure 16: PSV vector field for the air jet with (a) 5.6° and (b) 22° inclination, summed over 300 images.

effect caused by the out-of-plane motion.

The defocusing effect can be explained by estimating the out-of-plane displacement and the depth of field (DOF). For phosphorescence imaging, the aperture of the camera lens is usually widely open so as to gain a sufficient signal strength, which then leads to a very narrow DOF, which can be estimated by $4(1+1/M_0)^2 f^{\#2}\lambda = 70$ μm. Beyond this range, the particle image starts to lose focus and the size is proportional to the particle distance to the focusing plane. The DOF is only one third of the UV light sheet thickness $\sim$200 μm, measured with a knife edge and photodiode. For Mie scattering particle images produced by a pulsed laser, whether a particle remains in focus or not is only decided by on the particle's location when

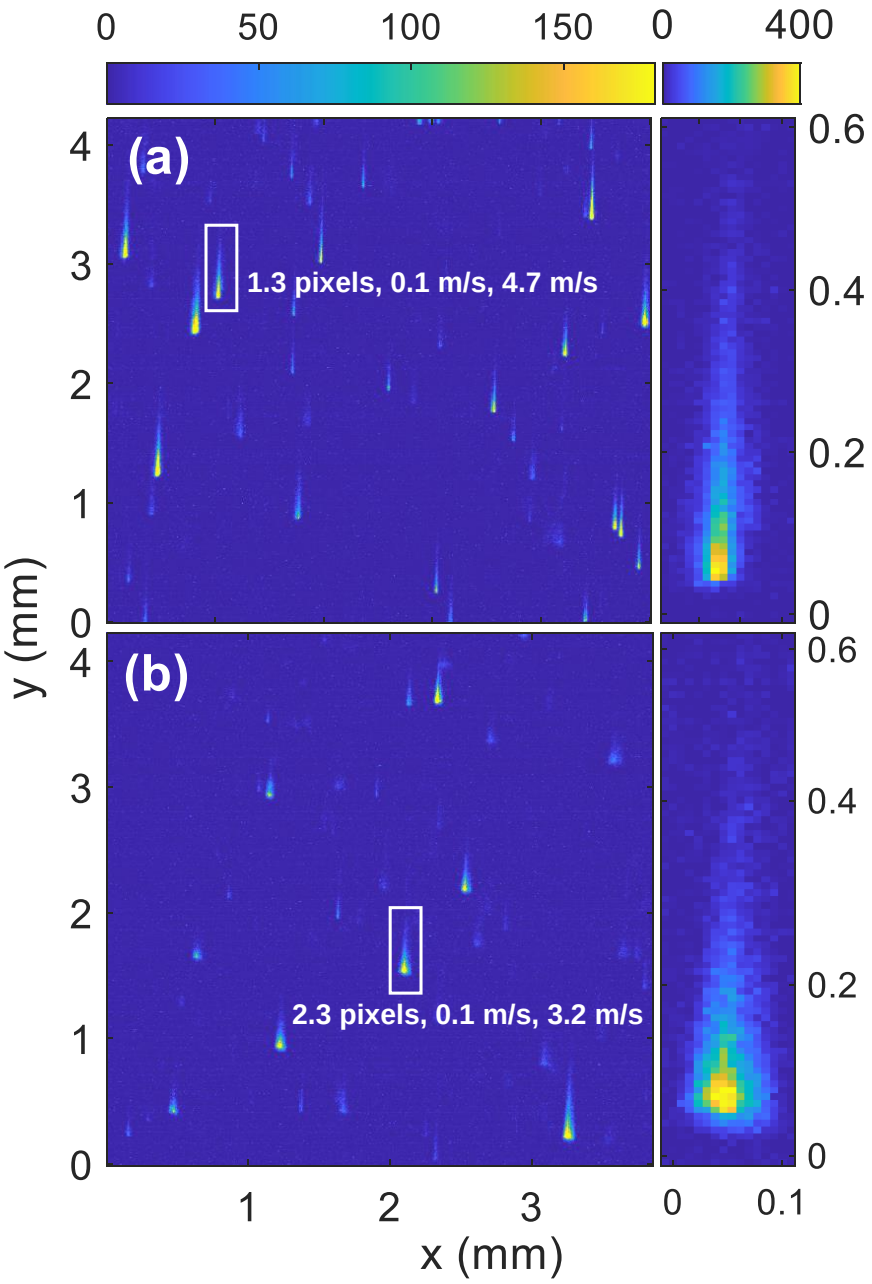

Figure 17: Example image acquired at (b) 5.6° and (b) 22° jet inclination towards the PSV camera, corresponding to 10% and 40% out-of-plane motion, respectively. An example streak, marked by the white rectangle, is enlarged and displayed on the right side for each case. The fitting result $[\sigma, v_x, v_y]$ for that streak is also presented.

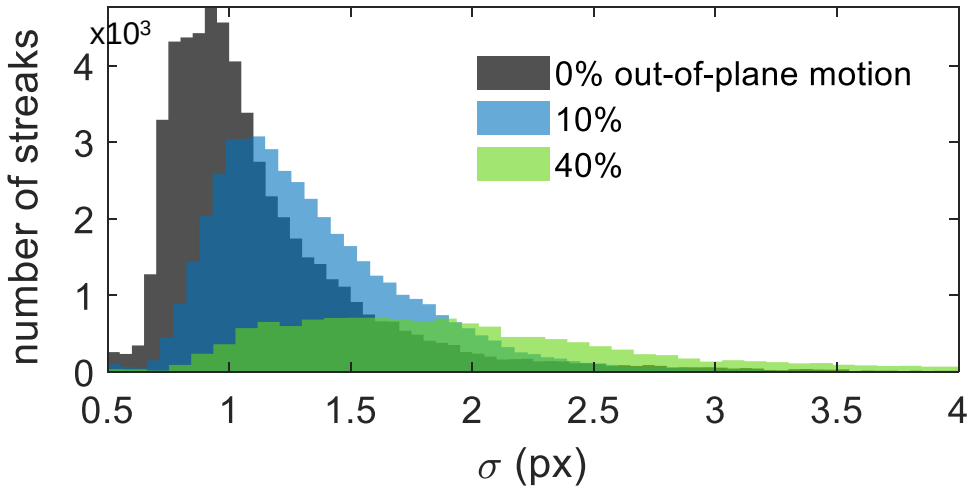

Figure 18: The histograms of streak size constant σ for 0%, 10%, and 40% out-of-plane motion.

illuminated. Hence, the proportion of out-of-focus particles does not depend on the flow motion, but only on the light sheet thickness relative to the camera depth of field (DOF). For phosphor-PSV, the situation is different as the particle continues to emit luminescence during its displacement. If the flow has a third velocity component normal to the light sheet, a particle initially residing within the DOF may move far out of the DOF at the end of its emission. However, in the streak evaluation we only consider a constant σ over time, hence for phosphor particles that are gradually losing focus as they move away from the DOF, the fitting in general reports a less focused streak, especially for those initially located at the edge of the DOF. Statistically, a wider distribution of σ can be expected for phosphor streak images acquired in flows with a stronger out-of-plane motion.

The histogram in Figure 18 for 0% out-of-plane motion has an edge at 0.6 px which can be taken as the size constant limited by both diffraction and aberration.

Based on geometrical optics, the blur circle is estimated using [19, 26]

$$d_e(z) = (M_0^2 d_p^2 + d_s^2 + d_a^2 + d_z^2)^{1/2} \tag{12}$$

with

$$d_z = \frac{M_0 z D_a}{z_0 + z} \tag{13}$$

where d_p is the particle physical diameter 1.94 μm, $M_0 = 0.64$ is the magnification factor; diffraction and aberration $(d_s^2 + d_a^2)^{1/2}$ together contribute $4\sigma = 2.4$ px (24.5 μm); the geometric particle image diameter due to defocusing $d_z = 16$ μm at $z = \pm 100$ μm, for an object distance $z_0 \approx 12$ cm and aperture size $D_a = 3$ cm. Hence the overall diameter of the blurred circle d_e counts for 29.3 μm (2.9 px) at the two edges of the light sheet. For a phosphor streak with an apparent length about 0.5 mm, as shown in Figure 17, 10% out-of-plane motion will lead to around 500 $\times$ sin5.6° = 49 μm inward or outward displacement, in the worst scenario case, a defocused tail with $\sigma = 3.4$ px can be expected. For 40% out-of-plane motion, however, the displacement increases to 188 μm, which falls far beyond the depth of field. For streaks obtained in such flow condition, the worst scenario case gives a defocused tail at $\sigma = 5.1$ px, although the signal will soon drop below the noise level as the photons are dispersed on a too large sensor area.

Our estimation on the upper bounds of σ for the three cases (2.9 px, 3.4 px, and 5.1 px) are validated by the histograms shown in Figure 18. This correlation sheds light on an interesting thought: for swirling flows, if a sufficient number of images has been acquired, the third component of the velocity field can be retrieved from the local PDF of the streak size constant σ, though with a direction ambiguity and on an average basis. Yet, to validate the idea, simultaneous stereo-PIV needs to be

performed, which is outside the scope of this paper.

6. Bias error caused by curved streaks

When choosing a phosphor for turbulent flow measurements, in addition to the range of mean velocity, the characteristic time scale of turbulence should also be considered. In the presence of small eddies in the flow, streaks may no longer appear straight, but exhibit considerable curvature, even though the flow velocity still falls within the right dynamic range for that phosphor. Figure 19 shows an example of curved streaks. The image was taken in the same Re = 55000 air jet as in Figure 8, but SMP:Sn^{2+} was used instead of BAM;Eu^{2+}. Curved streaks can be observed in both the jet core and the shear layer. For the two short bright streaks in the figure, despite their short length ($v\tau/\eta < 50$ px), which indicates the local velocity does not exceed the dynamic range, they still show a substantial curvature due turbulent motion in the mixing layer. Curved streamlines also cause problems for PIV and PTV, and thorough error analysis and a method to correct the velocity bias in such flows has been proposed in [27]. Here, when we extract the velocity using Eq. (2) in phosphor-PSV, components of velocity v_x, v_y are assumed to be constant during the measurement time, i.e., the decay time τ, and all analyses derived in Section 2.1 are built upon this assumption. Hence the effect of curved streaks on the PSV velocity retrieval is investigated in this section.

Figure 20(a) and (b) show two diagrams which illustrate the behaviour of PTV and of PSV in the case of varying velocity during the measurement time. For PTV or PIV, only the start and the end position of a particle is recorded, by which the displacement of the particle during the pulse interval is calculated. Hence, the resulting PTV vector represents an average velocity over the measurement time Δt. Yet, a first- and a second-order bias error in velocity measurement were still identified

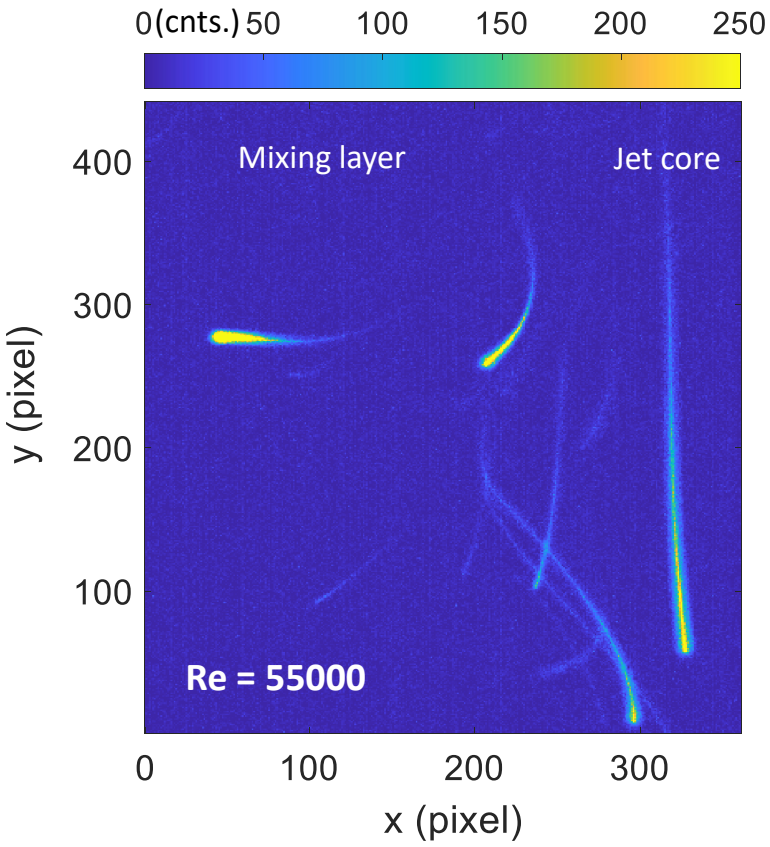

Figure 19: Streak images recorded in the mixing layer of the same Re = 55000 air jet in Figure 8, but SMP:Sn^{2+} ($\tau = 26.8$ μs) was used instead of BAM:Eu^{2+} ($\tau = 0.92$ μs).

in PIV/PTV measurements due to nonzero curvature streamline in the flow during the two laser pulses [27]. Of course, it is relatively easy to reduce the pulse interval in PIV/PTV to minimize the angular change in the velocity vector and thus reduce the bias error. However, it is limited by increasing uncertainty brought by the error in determining the exact particle position from a diffracted light spot, usually 5% of the particle image diameter [23]. In 2013, Cierpka et. al. [28] proposed a multi-frame (four frames in that study) PTV to determine the particle path, and thus to give more accurate velocity measurements and to reduce the positioning error caused by

vector reallocation in a flow field with curved streamlines.

Similarly, for a changing velocity field during the measurement time, PSV yields a vector pointing to a direction between V_0 and V_1, where V_0 is the initial velocity, and V_1 is the instantaneous velocity at $t = \tau$. However, since the phosphor emission intensity is decaying exponentially along the trajectory, the head of the streak is more influential in determining the recovered streak position and shape than the tail. As a consequence, the PSV vector is closer to the initial velocity V_0 comparing with the average velocity presented by PTV if $\Delta t = \tau$, as illustrated in Figure 20(b). Figure 20(c) shows a virtual curved Tin streak simulated by the finite time method, described in Section 2.7. While v_y remains a constant velocity at 0.4 px/μs, v_x accelerates at 0.02 px/μs^2 from 0 px/μs. Figure 20(d) presents the virtual streak based on the fitting result to (c). Comparing with the mean velocity $(V_0 + V_1)/2$, the retrieved vector is closer to the initial velocity V_1 in terms of both magnitude and angle, which validates our analysis illustrated in the PSV diagram. Therefore, applying the fitting method to curved streaks does not necessarily lead to a failure of fit or a nonphysical interpretation of the flow field.

To estimate the bias introduced by a changing velocity field quantitatively, we added a local acceleration $\boldsymbol{a}$ to a 1D flow. Two scenarios are considered: acceleration $\boldsymbol{a}$ is (a) along the flow direction, or (b) orthogonal to the initial flow direction, thus making the flow turn. The bias error was calculated based on the difference between the extracted velocity V relative to the initial velocity V_0. The result is plotted in Figure 21, where Δu denotes the velocity variation during the decay time τ, i.e., $\Delta u = \boldsymbol{a}\tau$. Clearly, in both scenarios, if the velocity variation during the decay time is less than 10% of the initial velocity to be measured, then the PSV method produces less then 5% bias error, and below 5° angular error (if the acceleration is normal to the initial flow direction). Otherwise, a phosphor with a shorter decay time τ may

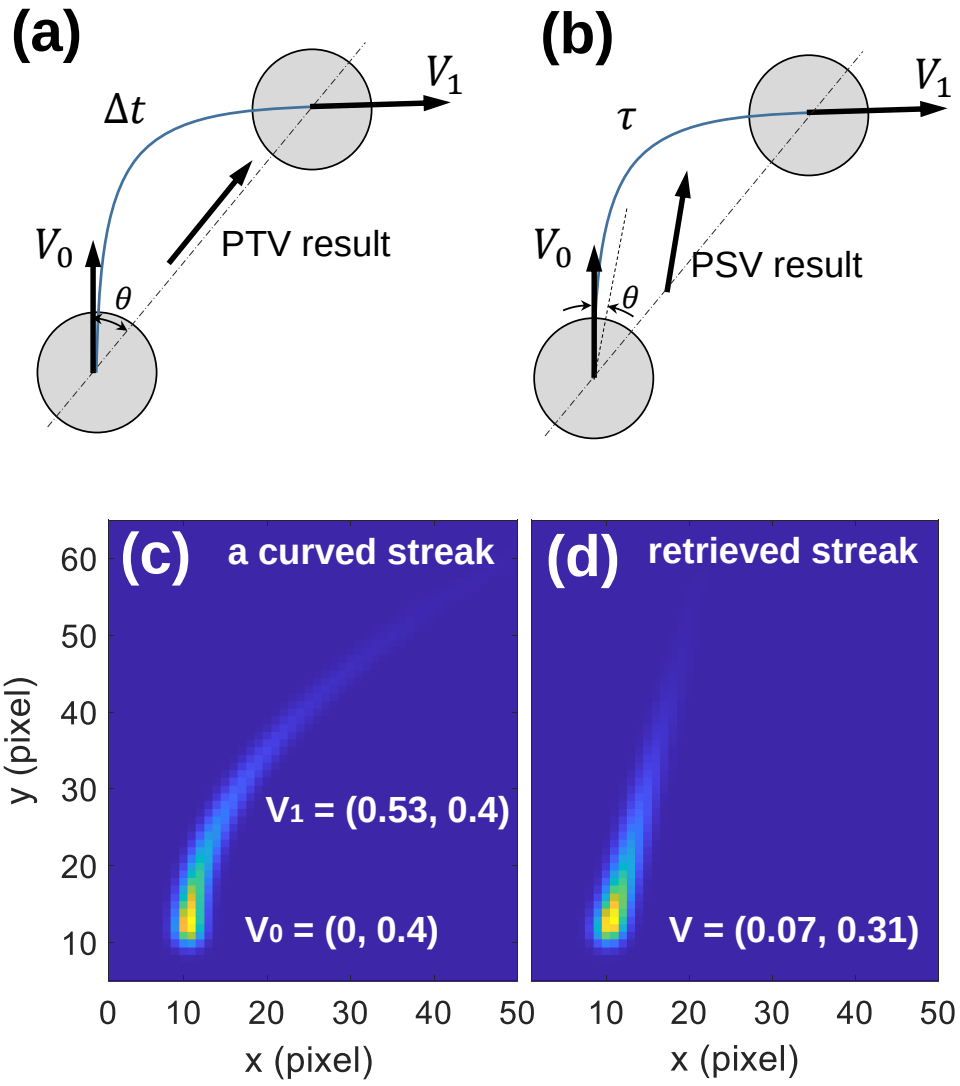

Figure 20: (a) A diagram of PTV behavior in the case of changing velocity during the measurement time, (b) behavior of PSV in the same case, (c) a noise-free curved streak simulated by the finite time method, the velocity unit is (pixel/μs), and (d) the retrieved streak based on the best fit to (c), assuming a constant velocity.

be chosen to further reduce Δu, meanwhile the spatial resolution should be further improved to maintain $v\tau/\eta$ in a detectable range for that phosphor.

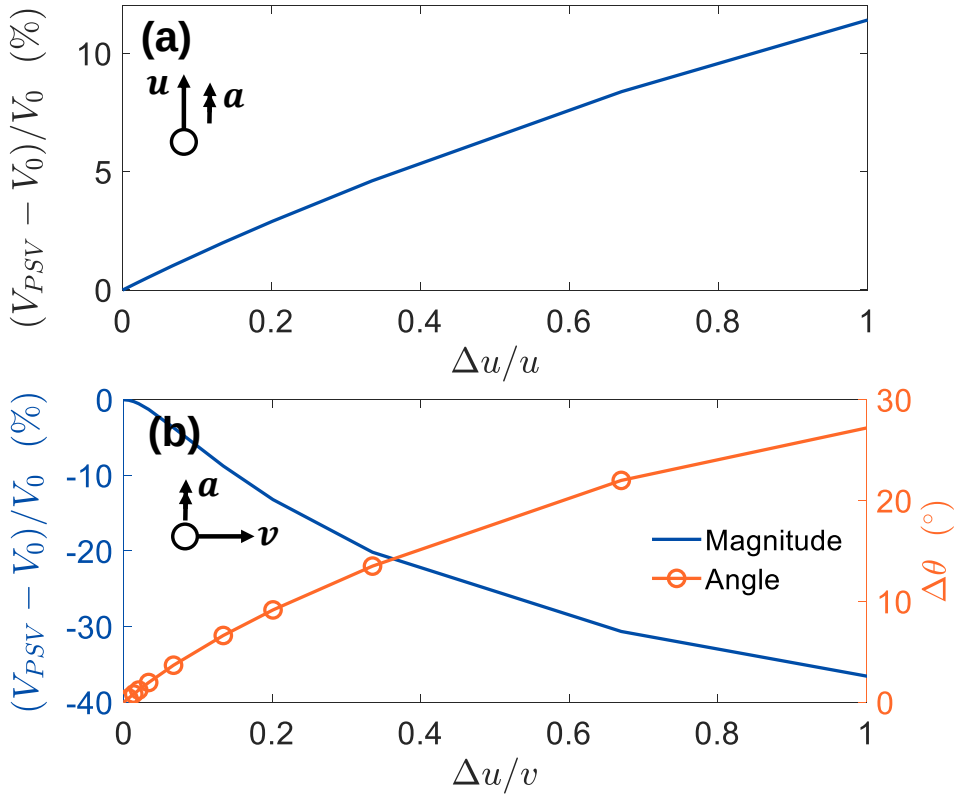

Figure 21: (a) Performance of PSV when an acceleration is added $\boldsymbol{a}$ along the direction of initial particle motion; (b) normal to the direction of initial particle motion. A curved streak will form in the latter case. Δu is the local velocity variation during the decay time τ, i.e., $\Delta u = \boldsymbol{a}\tau$

Unlike the light spots in a PIV image, curved streaks contain the valuable temporal information of the flow field. Theoretically, this information can be decrypted by incorporating the temporal emission curve of the phosphor, provided that the SNR is sufficiently high. However, extracting temporal velocity information is beyond the scope of this paper, here we only investigate the effect of curved streaks on the novel phosphor-PSV method.

7. Conclusions

The present paper extended our previous work [1] on a novel Phosphor Particle Streak Velocimetry (phosphor-PSV) technique that applied a 2D fit to individual phosphor streaks formed by the flow motion to extract the local flow velocity. In this study, a novel image dilation method was proposed for phosphor streak detection and segmentation at a much higher streak image density (0.004 spp) than the previously introduced window-based segmentation method (up to 0.001 spp). Phosphor-PSV was demonstrated using two other phosphors than the one selected in the previous work, targeting different flow conditions and velocity ranges. We extended the applicable flow velocity range demonstrated in our previous work (0.2-12 m/s) with the use of a slow decay phosphor GOS:Tb^{3+} which allowed to measure velocity fields in slow liquid flows ($<$ 20 cm/s), while BAM:Eu^{2+} was shown to be suitable for measurement up to 85 m/s. Comparisons on mean velocity profiles in the air jets among PSV, PIV, and hot-wire anemometry (HWA) [22] showed good agreement within the dynamic range of each phosphor, while PSV presented a higher rms error than PIV and HWA, as a technique based on individual particles.

A virtual streak approach was proposed to investigate the uncertainty and dynamic range of the PSV technique. Based on the simulation results, both the mean and the rms error in the velocity measurements was found to be less than 5% for streaks with a SNR $>$ 20, particle size constant $\sigma > 0.3$ px, and displacement $v\tau/\eta > 1$ px. Below those values, both mean and rms error increased quickly due to a low SNR or too few pixel intensities to enable a reliable fit. In particular, a too short or overly thin streak was found to be susceptible to the misalignment between the peak intensity and the pixel centre as well as to image defects in the streak images such as the aberration effect, which deviated the recorded intensity

distribution from the analytical streak model. Using the virtual streak approach, the dynamic range $v\tau/\eta = 0.8$-22 px was predicted for SMP:Sn^{2+} and was validated by the experiment results obtained in the laminar/transitioning jets. For phosphors with a higher emission intensity per particle, BAM:Eu^{2+} and GOS:Tb^{3+}, the theoretical maximum displacement reached 140 px and 730 px, respectively, although for too long streaks the streamline effect would appear depending on the magnitude of local vorticity. For any phosphor, a case by case study can be performed following the virtual streak approach, combining with the true emission data of that phosphor obtained from experiments. Alternatively, the goodness of fit R^2 was shown to be a good and quick measure to evaluate the uncertainty in each velocity vector, regardless of the phosphor used.

The effects of out-of-plane motion and curved streaks caused by small eddies were also investigated. Within 40% out-of-plane motion the PSV technique can still capture the in-plane velocities even if the imaged streaks were partially defocused; a less than 10% velocity variation during τ (a curved streak is formed if the velocity increment/decrement is normal to the initial flow direction) led to a less than 5% bias error and an angular error below 5°.

The new phosphor-PSV technique is a promising tool in exploring two-phase flows and those near solid boundaries. The 2D fitting technique for velocity extraction, the image dilation method for streak segmentation, as well as the uncertainty analysis by virtual streak synthesis presented in this study can be readily extended to a more general PSV approach or an even wider genre of velocimetry that does not limit to phosphor emissions, but potentially could use any decaying emission including pulsed-laser induced fluorescence, incandescence, or simply Mie scattering from a constant/modulated CW laser.

Acknowledgments

The authors gratefully acknowledge the financial support from Aero Futures Initiative, National Research Council Canada, and Professor Frank Beyrau at the Otto-von-Guericke University (OVGU) for access to equipment and laboratory. Help from Guangtao Xuan during the experiment at OVGU is also acknowledged.

Declarations

Competing interest. The authors have no relevant financial or non-financial interests to disclose.

Funding. This study is funded by the Aero Futures Initiative, National Research Council Canada.

Ethics approval and consent to participate. Not applicable.

Consent for publication. The authors hereby consent to publish this Work in the Experiments in Fluids.

Availability of data and materials. Data and materials that support the findings of this study are available on request from the corresponding author, B. Fond.

Authors' contributions. L. Fan conducted the experiments and simulations, as well as the data processing. P. Vena, B. Savard, and B. Fond conceptualised the study. All authors analysed the results and wrote the manuscript.

References

[1] L. Fan, P. Vena, B. Savard, G. Xuan, B. Fond, High-resolution velocimetry technique based on the decaying streaks of phosphor particles, Optics Letters 46 (2021) 641.

[2] C. J. Kähler, S. Scharnowski, C. Cierpka, On the uncertainty of digital PIV and PTV near walls, Experiments in Fluids 52 (2012) 1641–1656.

[3] D. Schanz, S. Gesemann, A. Schröder, Shake-The-Box: Lagrangian particle tracking at high particle image densities, Experiments in Fluids 57 (2016) 1–27.

[4] L. Fan, Y. Gao, A. Hayakawa, S. Hochgreb, Simultaneous, two-camera, 2D gas-phase temperature and velocity measurements by thermographic particle image velocimetry with ZnO tracers, Experiments in Fluids 58 (2016) 1–34.

[5] S. Someya, Y. Li, K. Ishii, K. Okamoto, Combined two-dimensional velocity and temperature measurements of natural convection using a high-speed camera and temperature-sensitive particles, Experiments in Fluids 50 (2011) 65–73.

[6] T. Yokomori, H. Nagai, H. Shiratori, N. Shino, N. Fujisawa, T. Hirasawa, Simultaneous Measurements of Phosphor Thermometry and PIV for High-Temperature Gas Flows, in: JSAE/SAE 2015 International Powertrains, Fuels & Lubricants Meeting, 2015, pp. 1–8.

[7] X. Bi, Z. Sun, T. Lau, Z. Alwahabi, G. Nathan, Simultaneous imaging of two-phase velocities in particle-laden flows by two-color optical phase discrimination, Optics Letters 46 (2021) 3861.

[8] J. Brübach, C. Pflitsch, A. Dreizler, B. Atakan, On surface temperature measurements with thermographic phosphors: A review, Progress in Energy and Combustion Science 39 (2013) 37–60.

[9] C. Abram, B. Fond, F. Beyrau, Temperature measurement techniques for gas and liquid flows using thermographic phosphor tracer particles, Progress in Energy and Combustion Science 64 (2017) 93–156.

[10] Z. Deng, J. König, C. Cierpka, A combined velocity and temperature measurement with an LED and a low-speed camera, Measurement Science and Technology 33 (2022) 115301.

[11] J. Bürbach, T. Kissel, M. Frotscher, M. Euler, B. Albert, A. Dreizler, A survey of phosphors novel for thermography, Journal of Luminescence 131 (2011) 559–564.

[12] B. Lecordier, J. Westerweel, The europiv synthetic image generator (s.i.g.), Particle Image Velocimetry: Recent Improvements (2004) 145–161.

[13] M. Stelter, Quantitative photoluminescence measurements of dispersed phosphor particles to improve optical thermometry in fluids, Master's thesis, Otto-von-Guericke-University Magdeburg, Germany, 2019.

[14] B. Fond, C. Abram, M. Pougin, F. Beyrau, Investigation of the tin-doped phosphor (Sr, Mg)$_3$(PO$_4$)$_2$:Sn^{2+} for fluid temperature measurements, Optical Materials Express 9 (2019) 802.

[15] Á. Yáñez González, Phosphorescent thermal history sensors for extreme environments, Ph.D. thesis, Mech. Eng, Imperial College, UK, 2015.

[16] C. Abram, B. Fond, A. L. Heyes, F. Beyrau, High-speed planar thermometry and velocimetry using thermographic phosphor particles, Applied Physics B 111 (2013) 155–160.

[17] B. Fond, C. Abram, M. Pougin, F. Beyrau, Characterisation of dispersed phosphor particles for quantitative photoluminescence measurements, Optical Materials 89 (2019) 615–622.

[18] B. Fond, C. Abram, F. Beyrau, Characterisation of the luminescence properties of bam:eu2+ particles as a tracer for thermographic particle image velocimetry, Applied Physics B 121 (2015) 495–509.

[19] R. J. Adrian, J. Westerweel, Particle Image Velocimetry, first edit ed., Cambridge University Press, Cambridge, 2011.

[20] T. Fuchs, R. Hain, C. J. Kähler, Non-iterative double-frame 2D/3D particle tracking velocimetry, Experiments in Fluids 58 (2017) 1–5.

[21] D. Witkowski, D. A. Rothamer, Investigation of aerosol phosphor thermometry (APT) measurement biases for Eu:BAM, Applied Physics B: Lasers and Optics 124 (2018) 202.

[22] L. Bogusławski, C. O. Popiel, Flow structure of the free round turbulent jet in the initial region, Journal of Fluid Mechanics 90 (1979) 531–539.

[23] A. K. Prasad, R. J. Adrian, C. C. Landreth, P. W. Offutt, Effect of resolution on the speed and accuracy of particle image velocimetry interrogation, Experiments in Fluids 13 (1992) 105–116.

[24] C. Cierpka, C. Kähler, Cross-correlation or tracking - comparison and discussion, 16th Int Symp on Applications of Laser Techniques to Fluid Mechanicsn, Lisbon (2012) paper No.299.

[25] M. Raffel, C. E. Willert, F. Scarano, C. J. Kähler, Particle Image Velocimetry A Practical Guide, 2018.

[26] M. G. Olsen, R. J. Adrian, Out-of-focus effects on particle image visibility and correlation in microscopic particle image velocimetry, Experiments in Fluids 29 (2000) S166–S174.

[27] S. Scharnowski, C. J. Kähler, On the effect of curved streamlines on the accuracy of PIV vector fields, Experiments in Fluids 54 (2013).

[28] C. Cierpka, B. Lütke, C. J. Kähler, Higher order multi-frame particle tracking velocimetry This article is part of the Topical Collection on Application of Laser Techniques to Fluid Mechanics 2012, Experiments in Fluids 54 (2013).